ISSN 0915-633X

NATIONAL INSTITUTE FOR FUSION SCIENCE

Simulation Study of MHD Dynamo:
Convection in a Rotating Spherical Shell

A. Kageyama, K. Watanabe and T. Sato

(Received – Jan. 11, 1993)

NIFS-207 Feb. 1993

RESEARCH REPORT
NIFS Series

NAGOYA, JAPAN

Simulation Study of MHD Dynamo: Convection in a Rotating Spherical Shell

A. KAGEYAMA[1]

Faculty of Science, Hiroshima University, Higashi Hiroshima 724, Japan

K. WATANABE and T. SATO

Theory and Computer Simulation Center, National Institute for Fusion Science, Nagoya 464-01, Japan

Abstract

Numerical simulations on the thermal convection of a neutral fluid (without the magnetic field) in a rotating spherical shell have been carried out. The results indicate that if the rotation is sufficiently rapid, the fluid results in a strong differential rotation where an equatorial acceleration is remarkable. The formation dynamics of convection columns aligned to the rotation axis is studied extensively. A new model of generation mechanism of the differential rotation is then proposed which concludes that the fluid motion generates an equatorial acceleration by selectively exciting the cyclonic columns in the spherical shell.

Keywords: dynamo, convection, differential rotation, computer simulation

[1]Now at Theory and Computer Simulation Center, National Institute for Fusion Science, Nagoya 464-01, Japan

1 Introduction

"Dynamo" may be one of the most mysterious mechanism in the frontiers of the magnetohydrodynamic (MHD) physics. The strong nonlinearity of the problem has compelled researchers to adopt rather rude approximations such as the kinematic dynamo model in which the feedback of the magnetic field to the fluid velocity is ignored. Recent remarkable development of computers, however, has enabled us to attack this highly nonlinear problem by means of the computer simulation.

The final goal of the present study is to invoke a comprehensive understanding of the dynamo mechanism with the belief that a non-turbulent, global ordered MHD flow induced in a rotating spherical shell can directly generate an ordered magnetic field like the earth's dipole field. Our main interest is the physics of the general MHD dynamo. We therefore do not exclude a priori the compressibility of the fluid which is ignored in the Boussinesq and anelastic approximations, but retain it in the belief that it would play some essential role in dynamo. The convection vessel considered here is a rotating spherical shell because this geometry is of special interest in connection with the planetary or stellar dynamo problem.

We divide the approach to revealing the MHD dynamo problem into two stages. The first is the study of the three-dimensional behaviors of the convection of a fluid without the magnetic field (neutral fluid). The effect of the magnetic field will be included subsequently. In this paper, we will report the results of numerical simulations of the thermal convection of a neutral fluid in a rotating spherical shell. The results of the simulation of the MHD fluid including the magnetic field will be reported in the future papers.

The thermal convection in a rotating spherical shell has so far been investigated through analytical [1, 2, 3], experimental [4, 5, 6, 7, 8, 9, 10] and numerical [11, 12, 13, 14, 15, 16, 17, 18] approaches. A common interest in these investigations is to explain the formation of the differential rotation on the sun and major planets where the fluid near the equator rotates faster than the rigid rotation of the celestial body. This phenomenon is known as the equatorial acceleration. Busse [2] pointed out that the differential rotation could be generated by nonlinear coupling of the velocity field. He has shown that the convection velocity is organized as a set of columnar cells because of the existence of the Coriolis force [1]. Gilman [11] has shown by the numerical simulation that the differential rotation takes the form of an equatorial acceleration when the rotation is sufficiently rapid. He argues that the kinetic helicity density is negative in the northern hemisphere. (Here and hereafter the north is defined as the direction of the rotation of the shell.) The above results are obtained under the Boussinesq approximation.

Gilman and Miller [15] performed a numerical simulation using an anelastic approximation [19] to study the effects of the density distribution in the spherical shell. Their major results are the same as those of the Boussinesq simulation.

These studies have led us to the understanding of many specific features of the rotating spherical shell convection. There remains, however, some important unresolved questions. Namely, what is the physical mechanism of the generation of the differential rotation? How is the differential rotation related to the velocity structure in the convection column?

The purposes of this paper is (a) to clarify the velocity configuration in the convection columns and (b) to propose a model of the generation mechanism of the differential rotation with a preferential equatorial acceleration.

2 Physical and Numerical Models

2.1 Geometry, governing equations and normalization

We consider an ideal gas confined between two concentric spherical boundaries. Both the inner and outer spherical boundaries are assumed to rotate with the same constant angular velocity $\mathbf{\Omega}$. We adopt the frame of reference rotating with the angular velocity $\mathbf{\Omega}$ (see the left panel of Fig. 1).

We normalize the variables by the following three parameters; the radius of the outer spherical boundary, the density and the temperature at the outer boundary. Denoting the normalized time, mass density, pressure, temperature and velocity by t, ρ, p, T and $\mathbf{v}$, respectively, the governing normalized equations are written as follows:

$$\frac{\partial \rho}{\partial t} = -\nabla \cdot (\rho \mathbf{v}), \tag{1}$$

$$\frac{\partial}{\partial t}(\rho \mathbf{v}) = -\nabla \cdot (\rho \mathbf{v}\mathbf{v}) - \nabla p + \rho \mathbf{g} + 2\rho \mathbf{v} \times \mathbf{\Omega} + \mu(\nabla^2 \mathbf{v} + \frac{1}{3}\nabla(\nabla \cdot \mathbf{v})), \tag{2}$$

$$\frac{1}{\gamma - 1}\rho(\frac{\partial}{\partial t} + \mathbf{v} \cdot \nabla)T = -p\nabla \cdot \mathbf{v} + K\nabla^2 T + \Phi, \tag{3}$$

with

$$p = \rho T, \tag{4}$$

$$\mathbf{g} = -\frac{g_0}{r^3}\mathbf{r}, \tag{5}$$

$$\Phi = 2\mu\left(e_{ij}e_{ij} - \frac{1}{3}(\nabla \cdot \mathbf{v})^2\right), \tag{6}$$

$$e_{ij} = \frac{1}{2}\left(\frac{\partial v_i}{\partial x_j} + \frac{\partial v_j}{\partial x_i}\right), \tag{7}$$

where $\gamma(=5/3)$, μ and K are the adiabatic constant, normalized viscosity and normalized thermal diffusivity, respectively. $\mathbf{r}$ is the position vector. g_0 is the gravity at the outer spherical boundary ($r=1$) and Φ is the dissipation function. e_{ij} is the stress tensor. The viscosity μ and the thermal diffusivity K are assumed to be constant. We ignore the self-gravity of the fluid and the centrifugal force. Using the equation of state (4), we can rewrite the thermodynamical equation (3) in the following way:

$$(\frac{\partial}{\partial t}+\mathbf{v}\cdot\nabla)p=-\gamma p\nabla\cdot\mathbf{v}+(\gamma-1)K\nabla^2T+(\gamma-1)\Phi. \tag{8}$$

Note that the normalized sound velocity at the outer boundary is $\sqrt{\gamma}\approx 1.29$.

2.2 Initial and boundary conditions

The initial condition is given by the hydrostatic and thermal equilibrium state:

$$T(r)=1-\beta+\frac{\beta}{r}, \tag{9}$$

$$\rho(r)=T(r)^m, \tag{10}$$

with

$$\mathbf{v}=0, \tag{11}$$

where $\beta>0$ is a constant and

$$m=\frac{g_0}{\beta}-1 \tag{12}$$

is the polytropic index [20].

The temperatures at both the inner (hot) and outer (cold) spherical boundaries are fixed. We adopt the stress-free boundary condition for the velocity.

2.3 Physical parameters

The system has six independent parameters; r_i (the radius of the inner sphere), μ (normalized viscosity), K (normalized thermal diffusivity), g_0 (gravity at the outer boundary), Ω (rotation rate of the shell) and m (polytropic index). Other important non-dimensional parameters which characterize the system are the Rayleigh number R, the Taylor number T and the Prandtl number P which are given by

$$R=\frac{g_0(\beta\frac{\gamma}{\gamma-1}-g_0)d^4}{\mu K}, \tag{13}$$

$$T=(\frac{2\Omega d^2}{\mu})^2, \tag{14}$$

and

$$P = \frac{1}{\gamma - 1}\frac{\mu}{K}, \tag{15}$$

where d is the depth of the shell ($d = 1 - r_i$). Note that the Rayleigh number of a stratified fluid is a function of the depth [20]. Here we measure the local Rayleigh number on the outer spherical boundary ($r = 1$) because we normalize the variables by the values on this boundary.

The physical parameters used in this study are as follows. $r_i = 0.5$, $\mu = 4 \times 10^{-4}$, $K = 1 \times 10^{-3}$, $g_0 = 0.4$ and $m = 1$. The local Rayleigh number and the Prandtl number for these parameters are 3.52×10^3 and 0.6. The remaining free parameter is the rotation rate of the shell Ω. We perform simulations for four different values of Ω; 0 (without the rotation), 0.1, 0.2 and 0.4. We concentrate mainly on the results of $\Omega = 0.4$ in this paper. The Taylor number is 2.50×10^5 for this case.

The density stratification is a specific feature for a compressible fluid in the gravity field. Note, however, that the density change in the spherical shell under the above parameters is small: The density at the inner boundary is only 1.15.

2.4 Coordinate system and numerical method

We numerically solve the equations (1), (2) and (8) as an initial value problem on the spherical coordinate system (r, θ, φ), where r is the radius ($0.5 \leq r \leq 1.0$), θ is the colatitude ($0 \leq \theta \leq \pi$) and φ is the longitude ($0 \leq \varphi < 2\pi$) (see the right panel of Fig. 1). The polar axis $\theta = 0$ is the direction of $\mathbf{\Omega}$. We shall call the plane $\theta = \pi/2$ as the equatorial plane.

We solve the above set of equations without any ad hoc assumptions, keeping the full compressibility of the fluid. We, therefore, have the sound wave mode as well as the convection mode. The maximum speed of the convection is about 1% of the sound speed under the above physical parameters.

We use the second-order finite difference in all (r, θ and φ) directions. The total grid number is 20 (radial) $\times$46 (latitudinal) $\times$128 (longitudinal) for all the simulation runs. The latitudinal grid spacing is $\Delta\theta = 3.9°$ and the longitudinal grid spacing is $\Delta\varphi \approx 2.8°$. Simulations indicate that the convection velocity is organized as a set of many elongated columns aligned to the rotation axis. Thus the finer grid mesh in the longitudinal direction than that in the latitudinal direction is required.

We adopt the fourth-order Runge-Kutta-Gill (RKG) scheme for the time integration [21, 22]. The length of the time step is determined by the Courant-Fridrich-Levi condition: $\Delta t = 7.1 \times 10^{-3}$.

There are two numerical difficulties to solve the finite difference equations on the spherical coordinate system. The difficulties and the numerical techniques developed to overcome them are given in Appendix.

We begin the simulation run by adding a random temperature perturbation to the initial equilibrium. Convective flows are excited by the perturbation since the initial condition is unstable. We execute the time development of the convections for a sufficiently long time (about 5.7 thermal diffusion time in the typical case).

3 Simulation Results

3.1 Formation of convection columns

The best way to reflect the effects of the rotation on the convection motion in the spherical shell is to compare the saturated convection patterns of the two cases with and without the rotation. The two panels in Fig. 2 show the velocity field on a spherical cross section of radius $r = 0.75$ (the middle of the spherical shell) for the case of $\Omega = 0$ (upper panel) and for $\Omega = 0.4$ (lower panel). The contour line denotes the radial component of the velocity. The solid line illustrates the rising (up-going) fluid region and the dashed line the sinking (down-going) fluid region. All physical parameters in both cases are the same except for the rotation rate. When the rotation is absent, the system is spherically symmetric so that the convection cells have, of course, no preference for a particular direction. On the other hand, when the shell is rotating, convection cells are elongated and alinged to the rotation axis [1]. We call them "convection columns" in this paper.

Although the initial temperature perturbation, which is imposed randomly, is not necessarily symmetric about the equator, Fig. 2 indicates that the saturated convection pattern is symmetric about the equator [1].

Hereafter we will mainly investigate the convection for the case of $\Omega = 0.4$.

3.2 Temporal evolution of energy and helicity

In order to outline the evolution of the convection, we first show the time history of the total volume integral of several quantities over the whole spherical shell. Fig. 3 shows the time development of the volume integral of the kinetic energy (thick line), the differential rotation kinetic energy (thin line) and the absolute value of the kinetic helicity density. (Because the saturated convection motion is almost perfectly mirror symmetric about the equatorial plane,

the kinetic helicity density distribution is anti-symmetric about the equator. Therefore, the total integration of the helicity density itself vanishes.) The x-axis is the number of the time steps. The left side scale in Fig. 3 is for the energy and the right side is for the helicity.

Before we examine the time evolution we summerize several characteristic time scales in this system. Among them, the sound wave time scale is the shortest one. It takes about d/v_s to cross the shell depth $d(= 0.5)$ for the sound wave, where v_s is the sound velocity. Since the temperature difference in the shell is small, we evaluate v_s at the outer boundary; $v_s = \sqrt{\gamma} \approx 1.29$. Then the sound wave transverse time $\tau_{sound} \approx 3.88 \times 10^{-1}$ (about 55 time steps). The thermal diffusion time is $\tau_{therm} = d^2/K/(\gamma - 1) = 3.75 \times 10^2$ in normalized unit (about 53,000 time steps). The total time steps of this run are 300,000. The viscous dissipation time is greater than the thermal diffusion time by factor 1/0.6 which is the reciprocal of the Prandtl number. The period of the rotation of the spherical shell is $\tau_{rot} = 2\pi/\Omega = 1.57 \times 10^1$ (about 2,200 time steps). The remaining time scale is the circulation time of a convection cell. We cannot evaluate this time scale until we execute the actual run. It turns out that after the convection saturates the convection velocity v_c reaches to 1.33×10^{-2}, which is about 1% of the sound velocity at the outer boundary. The circulation time is therefore $\tau_t = 2d/v_c \approx 7.52 \times 10^1$ (about 11,000 time steps).

It is seen in Fig. 3 that the total kinetic energy (TKE) grows exponentially in the initial linear phase and it reaches a peak at about 30,000 time steps. After about one thermal diffusion time, the convection saturates and reaches to an almost stationary state.

The helicity (H) grows in accordance with the kinetic energy. The helicity and the kinetic energy reach to their peaks at the same time (about 30,000 time steps).

The differential rotation energy (DRE) develops with a certain time delay against the growth of the total kinetic energy. This is due to the fact that the differential rotation is generated by the nonlinear coupling of the velocity. It should be noted in Fig. 3 that the differential rotation kinetic energy reaches about one third of the total kinetic energy when the convection saturates.

3.3 Profile of temperature, density and pressure

Before we go on to describe the behaviors of the velocity field, we shall briefly look at the thermodynamical properties of the convection. Fig. 4 shows the thermodynamical properties at the equatorial cross section at 300,000 time steps. The maximum velocity at this time is 1.33×10^{-2}. The upper left panel indicates the contours of the temperature and the upper

right panel the contours of the density. The lower right panel indicates the contour of the pressure perturbation. For the sake of comparison, we show the θ-component of the vorticity in the equatorial plane in the lower left panel. The solid contour line represents the positive (southward) part and the dashed contour line the negative (northward) part. The spherical shell is rotating in the counterclockwise direction.

The lower left panel indicates that there are seven pairs of cyclonic and anticyclonic columns. Here the cyclonic column is a convection column in which the fluid rotates in the cyclonic direction, i.e., the same direction of the spherical shell rotation. The fluid in the cyclonic column has a northward vorticity and the fluid in the anticyclonic column has a southward vorticity.

The temperature and density perturbations caused by the convection motion are non-negligible so that there appear sizable distortions on their contours as seen in Fig. 4. Note, however, that the compressible effect is not essential at all as far as the convection dynamics is concerned. We believe that the compressibility would play some essential role when the magnetic field dynamics is included in future.

The lower right panel of Fig. 4 shows a characteristic profile of the pressure perturbation of a rotating fluid. This figure indicates that the pressure of the fluid in the cyclonic column is low and the pressure in the anticyclonic column is high. This is explained by a geostrophic balance between the pressure and the Coriolis force [23].

3.4 Time development of convection columns

In this subsection, the temporal evolution of the convection columns is outlined from the start-up of the convection until the end of the run. Fig. 5 shows the radial component of the velocity at the middle of the spherical shell ($r = 0.75$) at 10, 20, 40, 100 and 200 thousand time steps. (The lower panel of Fig. 2 is at 300 thousand time steps of the same run.) Note that the scale of the contour lines is changed in each time step to visualize the early stage of the faint convection pattern.

There are four pairs of columns at $10,000$ time steps. Although the growing convection pattern is almost perfectly symmetric about the equator, we can see the remnant of the asymmetric components. The columns are divided into thinner five pairs of columns until $20,000$ time steps when the convection is still at the initial growing stage. Although the convection energy reaches a peak at about $30,000$ time steps (see Fig. 3), the internal structure of the columns still keeps changing. The middle panel of Fig. 5 at $40,000$ time steps shows a transient

stage when the column pair number is decomposed into seven from the early four columns at 10,000 time steps. The cascade of the column decomposition ends at this mode number seven.

Shown in Fig. 6 are the power spectra of the longitudinal mode of the radial velocity component v_r in the equator at 30,000 time steps (upper panel) and 300,000 time steps (lower panel). The time development of four modes (longitudinal mode number $m = 4, 5, 6$ and 7) are illustrated in Fig. 7, which clearly indicates the tendency that the kinetic energy converges into the single mode $m = 7$ (along with the higher harmonic $m = 14$).

The columns are slowly drifting in the longitudinal direction. In order to elucidate the longitudinal drift of the columns, we show in Fig. 8 the temporal development of the radial component of the velocity v_r in the equator. The x-axis is the longitude (thus periodic) and the y-axis is the time steps. The black region corresponds to $v_r > 0$ (rising fluid) and the white region $v_r < 0$ (sinking fluid). This figure clearly shows the change of the number of the convection columns and the longitudinal drifts of the columns. An interesting finding in this figure is that the columns drift eastward until the convection saturates (about 30,000 time steps) and then they drift westward. The westward drift velocity is about 2° per rotation of the spherical shell.

3.5 Velocity near the outer boundary

Let us now examine the saturated velocity field near the outer boundary. Shown in Fig. 9 are the spherical cross sections of radius $r = 0.9$ at 300,000 time steps. The horizontal components of the velocity are shown by arrows in the upper panel and the radial components are shown in the lower panel.

Seven pairs of the cyclonic and anticyclonic columns are observable. The first column from the left is an anticyclonic column. It should be noted in the upper panel that the cyclonic columns are larger in size than the anticyclonic columns. As a result of the difference of the column sizes, a net eastward zonal flow is generated near the equator and a westward zonal flow at the high latitude region. In this way, an equatorial acceleration is generated.

Comparison of the behaviors of the horizontal and radial flows in Fig. 9 indicates that there must exist the velocity component parallel to the rotation axis Ω. The fluid in the anticyclonic column "rises" from the equator toward both the northern and southern ends of the column and then the fluid in the cyclonic column "sinks" from both ends toward the equator. This is confirmed by the contour lines of radial component of the velocity field (the lower panel). Hereafter, we shall call this fluid flow along the column axis as the axial flow

circulation in the direction of Ω. The direction of the axial flow circulation indicates that fluid parcels in both the cyclonic and anticyclonic columns experience the left-handed helical trajectories in the northern hemisphere and the right-handed helical trajectories in the southern hemisphere [24]. The fluid, therefore, has a negative helicity in the northern hemisphere and a positive helicity in the southern hemisphere.

Another remakable feature observed in Fig. 9 is the crescent shape of the convection patterns (see the lower panel). It is to be emphasized that the bending of the convection pattern in the spherical cross section does not mean that the convection columns themselves are bended. We will show in section 3.7 that the convection columns are certainly straight in the direction of Ω. The reason that despite the straight columns the contour lines exhibit the bending structure will be explained in the next subsection.

3.6 Velocity in the equatorial plane

The left panel of Fig. 10 shows the velocity field in the equatorial plane. The spherical shell rotates in the counterclockwise direction in this figure. Because of the north-south symmetry of the convection motion, the θ-component of the velocity at the equator remains to the level of the initially given small perturbation level. It is evident that seven pairs of the cyclonic and anticyclonic columns are generated.

The asymmetry between the cyclonic and anticyclonic columns is obvious in this panel. The cyclonic columns are much larger than the anticyclonic columns. Thus, there remains a net eastward flow near the outer boundary. This eastward mean flow is also evident in the spherical cross section near the outer boundary (r=0.9; Fig. 9).

In the left panel of Fig. 10 it is clearly seen that the cross section of each column at the equatorial plane is not a rectangle but is close to a parallelogram [25]. Each cross section tilts to the longitudinal direction. The column extends straight in the direction of Ω with the same cross section of parallelogram due to the Taylor-Proudman theorem [26]. The crescent-like appearance of the convection pattern shown in Fig. 9 merely reflects the tilting characteristic of the column's cross section. The direction of the tilt of the column's cross section determines the direction of the bend of the convection pattern seen in the spherical cross section.

The right panel of Fig. 10 shows a cross section of equi-latitudinal plane which is 20° northward from the equatorial plane. The contour is the θ-component of the velocity. The solid lines denote the positive (southward) component and dashed lines denote the negative (northward) components. These contour lines indicate that, in the northern hemisphere, the

fluid in the cyclonic column flows from the northern end toward the equator and the other way round in the anticyclonic column. This panel indicates us that the fluid circulates in each column in the direction of Ω.

In the cyclonic column, the fluid "sinks" from both the northern and southern ends toward the equator. They collide at the equator and form a combined flow which wells out from the cyclonic column and then merge into the anticyclonic column. The fluid, which merges into an anticyclonic column at the equator, "rises" or "emerges" through the anticyclonic column from the equator towards the northern and southern ends.

3.7 Flow line in convection columns

In order to investigate the three-dimensional flow structure in the columns we show an example of a flow line traced at 200,000 time steps. Fig. 11 shows the three-dimensional display of a flow line (white) in the northern hemisphere viewed from four different directions. The flow line is traced over the length of 12.5. The brown sphere in the figure denotes the inner boundary and the greenish disk, which spans between the inner and the outer boundaries, is the equatorial plane. The color on the disk shows the θ-component of the vorticity ω_θ in the equatorial plane. The red region denotes the positive ω_θ (southward vorticity) and the blue region denotes the negative ω_θ (northward vorticity). The upper-left panel shows the view from the the direction of $\theta = 0$, or from the north. The upper-right panel and the lower-left panel are the views from the directions of $\theta = 30°$ and $\theta = 60°$. The lower-right panel is the view from $\theta = 90°$ in which the equatorial disk becomes a line. The view from the due north (upper-left) clearly indicates that the flow consists of a large vortex cyclonic column and a small vortex anticyclonic column aligned to the rotation axis and that they are continuously connected.

3.8 Helicity and differential rotation

Fig. 12 shows the meridional cross sections of the longitudinally averaged helicity density contours (left) and the differential rotation contours (right) at 300,000 time steps. The helical flow in each column generates a negative helicity (dashed lines) in the northern hemisphere and a positive helicity (solid lines) in the southern hemisphere. The contour lines of the helicity density support the fact that the columns are straight and extend along the direction of Ω. The anti-symmetrical distribution of the helicity density in the northern and southern hemispheres reflects the mirror-symmetry of the convection motion about the equator. The maximum value of the helicity density is 8.48×10^{-4} and the minimum value is -8.48×10^{-4}.

The right panel of Fig. 12 shows the meridional profile of the axially symmetrical component of the longitudinal velocity $\overline{v}_\varphi$, i.e., the differential rotation. The solid line denotes the positive $\overline{v}_\varphi$ and the dashed line denotes the negative $\overline{v}_\varphi$. The fluid in the solid contour region rotates faster than the rotation of the boundary spheres. The contour lines are nearly parallel to the rotation axis. This also reflects the fact that the columns are straight in the direction of the rotation axis. The distortion of the contour lines near the inner boundary indicates the existence of the transverse flow which connects the cyclonic column to the anticyclonic column in the west side (see the left panel of Fig. 10).

$\overline{v}_\varphi$ in the meridional plane increases with the distance from the rotation axis. The peak, at which $\overline{v}_\varphi = 2.95 \times 10^{-3}$, is located at the outer boundary in the equatorial plane (the outermost point from the rotation axis.) We note that the maximum velocity of the convection motion at this time is 1.33×10^{-2}.

Regarding the zonal flow or the equatorial acceleration observed on the sun and major planes, it is interesting to see how the differential rotation changes as a function of latitude. Fig. 13 indicates that the fluid near the equator ($60° < \theta < 120°$) rotates faster than the rigid rotation of the boundary spheres while the fluid in the high latitude region (($0° < \theta < 45$, $135° < \theta < 180°$) rotates slower than the rigid rotation. This result confirms that the equatorial acceleration is generated and maintained by the thermal convection in a rotating spherical shell.

3.9 Axial flow circulation in columns

Why is the helicity negative in the northern hemisphere and positive in the southern hemisphere? In other words, what determines the direction of the axial flow circulation in the cyclonic and anticyclonic columns? In order to answer this question, we shall consider the driving mechanism of the axial flow circulation.

The axial circulation is caused by the gradient of the geostrophic pressure perturbation along the column axis, $-\nabla_\parallel p'$, which originates from the difference of the Coriolis force between the equator and the northern and southern ends of the columns.

In the stationary state, the amplitude of the velocity is almost the same from the equator toward the ends of the columns (see Fig. 12). This reflects the Taylor-Proudman theorem which states that the velocity field does not vary in the direction of Ω. Therefore, the nonuniformity of the Coriolis force in the columns is not due to the change of the velocity amplitude.

The real reason that the Coriolis force near the northern and southern ends of the columns is weakened is the following. It is the curvature of the spherical outer boundary.

Although the convection motion in the equatorial plane is perpendicular to Ω, the velocity near the ends of the columns is almost parallel to the outer boundary (see Fig. 11), hence, the effective Coriolis force is diminished. Therefore, the pressure is more strongly modulated (high in the anticyclonic column and low in the cyclonic column) at the equator than near the ends of the columns. Consequently the axial flow circulation in the direction described above is driven in the columns.

3.10 Effects of rotation rate

The above results indicate that the generation of the kinetic helicity and the differential rotation are closely related to the formation of the columns alinged to Ω which is a consequence of the Coriolis force. It is, therefore, interesting to compare the results of $\Omega = 0.4$ with smaller rotation rates. Shown in Fig. 14 are the mean helicity density (left panel) and the differential rotation (right panel) in the meridional plane in the case of $\Omega = 0.2$ at $200,000$ time steps. Other physical parameters are the same. The Taylor number is 6.25×10^4.

The left panel indicates that the fluid exhibits a helical trajectory and constitutes a columnar cell structure. The north-south symmetry about the equator is reserved. However, the contour lines are inclined along the spherical boundaries (compare with the left panel of Fig. 12). The helicity distribution is, as a whole, shifted toward the northern and southern poles. This implies that the columns are not straight in the direction of Ω. The fluid in the columns can enter into the high latitude region because the columns are fairly bent in this case. The right panel of Fig. 14 shows that the equatorial acceleration is not generated at all. Rather an equatorial deceleration is observed.

Fig. 15 shows the results for $\Omega = 0.1$ at $200,000$ time steps. The Taylor number is 1.56×10^4. The symmetry about the equator is broken. The profiles of both the helicity and the differential rotation are badly correlated. This indicates the ineffectiveness of the constraint of the rotation on the convection motion in this low rotation rate.

4 Generation Mechanism of Differential Rotation

In this section, we describe the generation mechanism of the differential rotation which exhibits the equatorial acceleration.

4.1 Differential rotation and convection columns

Here we briefly summarize the relation between the differential rotation and the symmetry of the columns. Fig. 16 shows the schematic diagrams of three kinds of the equatorial cross sections of the columns. The curvature of the inner and outer spherical boundaries are ignored (compare with Fig. 10). In the top panel of Fig. 16, the cyclonic column and the anticyclonic column have the same size and are located one after another. As one can see in this panel, there should be no differential rotation because the longitudinal velocity component in the cyclonic (rotating counter-clockwise) column and that in the anticyclonic (rotating clockwise) column cancel out with each other.

As we have seen in Fig. 10, the equatorial cross section of each column tilts in the longitudinal direction like a parallelogram. The middle panel of Fig. 16 shows the tilted cross sections of the columns. One can see from this panel that the longitudinal velocity component in the cyclonic column and that in the anticyclonic column cancel out with each other as is seen in the top panel. Therefore, any differential rotation is not formed in this case. Thus we can conclude that the tilt of the column is not related to the differential rotation.

The necessary condition for the generation of the differential rotation must lie in the asymmetry of the column sizes (see the bottom panel of Fig. 16). Because the cyclonic column is greater in size than the anticyclonic column, the fluid ends up generating a resultant differential rotation shown in Fig. 12.

4.2 Symmetry breaking of the convection columns

Gilman [12] and Gilman & Miller [15] have shown by analizing the angular momentum transport that the differential rotation which takes the form of the equatorial acceleration is generated by the Reynolds stress, i.e., the nonlinear coupling of the velocity field. In their results, however, the physical mechanism of the differential rotation generation was not addressed. In this subsection, we will explain how the nonlinear coupling of the velocity causes the differential rotation, in other words, how the nonlinear coupling of the velocity breaks the symmetry of the columns.

We must first emphasize the necessity of the axial flow circulation in each column for the generation of the differential rotation. If the axial flow circulation in the direction of Ω does not exist, the convection motion is essentially two dimensional. In this case, the effect of the Coriolis force appears only in the pressure through the geostrophic balance [27]. Consequently, the sizes of the cyclonic and anticyclonic columns remain the same in the two-dimensional

flow. Therefore, the axial flow circulation is concluded to be essential for the generation of the differential rotation.

The differential rotation is closely related to the longitudinally averaged vorticity $\overline{\boldsymbol{\omega}}$ as follows. (Here we use the cylindrical coordinate system (R,ϕ,z).)

$$\overline{\omega}_R = -\frac{\partial \overline{v}_\varphi}{\partial z}, \tag{16}$$

$$\overline{\omega}_z = \frac{1}{R}\frac{\partial}{\partial R}(R\overline{v}_\varphi), \tag{17}$$

where $\overline{v}_\phi$ is the longitudinal average of v_φ. Fig. 17 shows $\overline{\boldsymbol{\omega}}$ in the meridional plane at 300,000 time steps when $\Omega = 0.4$. The formation of the differential rotation which exhibits the equatorial acceleration (Fig.12) is equivalent to the generation of the northward vorticity flux shown in Fig. 17. This is the problem of "vorticity dynamo".

Here let us consider a simplified model. We concentrate on the region near the equatorial plane. Ignoring the curvature of the spherical boundaries, we use a cartesian coordinate system. The equatorial plane corresponds to $z = 0$. A fluid is confined in a layer which is surrounded by the stress-free boundaries located at $y = 0$ and $y = \pi$. Both the gravity and the temperature gradient direct towards the negative y direction. The whole system is rotating about the z-axis with a constant angular velocity $\boldsymbol{\Omega} = (0, 0, \Omega)$. We suppose that the system is periodic in the x-direction.

In the initial linear stage, the cyclonic and anticyclonic columns can be assumed to be symmetric. The helical flow in the columns can be written as follows.

$$\mathbf{v} = \mathbf{v}_0 + \epsilon\, \mathbf{v}_1, \tag{18}$$

where $\mathbf{v}_0$ is the two-dimensional convective motion in the x-y plane and $\mathbf{v}_1$ denotes the axial flow circulation component in the columns. ϵ (> 0) is a small constant and $O(\epsilon^2)$ will be ignored. We suppose

$$\mathbf{v}_0 = (\partial_y \psi, -\partial_x \psi, 0)\,, \tag{19}$$

$$\mathbf{v}_1 = (-\partial_x \psi, 0, -z\psi)\,, \tag{20}$$

where

$$\psi = \sin x \sin y. \tag{21}$$

The helicity density $h = \mathbf{v}\cdot\boldsymbol{\omega} = -2\epsilon z(\sin^2 x + \sin^2 y)$ is negative in $z > 0$ and positive in $z < 0$.

Let us now evaluate the sign of the vorticity generation rate $\nabla \times (\mathbf{v} \times \boldsymbol{\omega})$ at the column boundaries $x = 0$ and π where $\omega_z = 0$. Then we obtain

$$\int_0^\pi [\nabla \times (\mathbf{v} \times \boldsymbol{\omega})]_z dy \;=\; \partial_x \int_0^\pi (\mathbf{v} \times \boldsymbol{\omega})_y dy - [(\mathbf{v} \times \boldsymbol{\omega})_x]_{y=0}^{y=\pi}$$

$$= \epsilon\partial_x \int_0^\pi \left(-\cos^2 y \sin x \cos x + 2\sin^2 y \sin x \cos x\right) dy$$
$$= \frac{\epsilon\pi}{2}\cos(2x). \tag{22}$$

Therefore, the vorticity generation rate is positive at $x = 0$ and $x = \pi$. Consequently, the cross sectional area of the cyclonic column increases as a result of the nonlinear coupling of the velocity field.

Although the cross sectional areas of the positive and negative ω_z fluxes can be changed by this process, the total vorticity flux is not changed (see (22)) because the vortex stretching and folding (the term $\nabla \times (\mathbf{v} \times \boldsymbol{\omega})$), which change the local vorticity distribution in the fluid, cannot produce any net total vorticity flux.

The generation rate of the total vorticity flux Ψ is given by

$$\frac{d\Psi}{dt} = \int \frac{\partial \boldsymbol{\omega}}{\partial t} \cdot d\mathbf{S}$$
$$= \oint \frac{\partial \mathbf{v}}{\partial t} \cdot d\boldsymbol{\ell}, \tag{23}$$

where $d\mathbf{S}$ and $d\boldsymbol{\ell}$ are the surface element and the line element, respectively. Equation (23) indicates that the total vorticity flux is generated by the fluid acceleration at the boundaries through the interaction between the fluid and the boundaries.

Therefore, the process of the differential rotation generation, which is expressed as the northward total vorticity flux generation, can be divided into two steps: (i) the inflation (deflation) of the cyclonic (anticyclonic) columns due to the axial flow circulation; (ii) net vorticity flux generation due to the buoyancy acceleration at the boundaries.

In the first step, the cross sectional area of the cyclonic column increases but the total northward vorticity flux within it does not change. This means that the fluid velocity in the cyclonic column is "adiabatically" reduced or weakened while the velocity in the anticyclonic column is intensified. The slowed convection motion in the cyclonic column is accelerated by the buoyancy force in order to convey the heat from the hot boundary to the cold boundary. Obviously, this buoyancy acceleration operates asymmetrically between the cyclonic and anticyclonic columns. This is the second step which can be expressed as the smoothing of asymmetrically distributed velocity between the cyclonic and anticyclonic columns caused by the first step. Consequently, the net northward vorticity flux is generated or injected through the boundaries.

5 Summary

In a rotating spherical shell convection, the velocity is organized as a set of convection columns alinged to the rotation axis Ω because of the constraint of the Coriolis force. If the rotation is sufficiently rapid, the columns extend straight in the direction of Ω. This configuration inevitably causes the axial flow circulation along the column axis. The combination of the axial flow circulation and the rotating convective motion produces a negative kinetic helicity in the northern hemisphere and positive helicity in the southern hemisphere.

The differential rotation which takes the form of equatorial acceleration is expressed as the mean northward vorticity flux. The generation of the differential rotation can, therefore, be rephrased as a vorticity dynamo problem.

The cyclonic column has a northward vorticity flux and the anticyclonic column has a southward vorticity flux. Therefore, the spherical shell is filled with pairs of the vorticity fluxes with opposite polarities. If the cyclonic column and the anticyclonic column are perfectly symmetric, the total vorticity flux is zero since both fluxes cancel out with each other. The equatorial acceleration is a consequence of the fact that the northward vorticity flux in the cyclonic column glows more effectively than the southward vorticity flux in the anticyclonic column.

The axial flow circulation in each column inflates the cyclonic columns and deflates the anticyclonic columns due to the nonlinear coupling of the velocity field. The vorticity flux, however, cannot be generated by this process because it is merely a vortex stretching and folding. The inflation of the cyclonic column reduces the velocity in the cyclonic column while the velocity in the anticyclonic column is intensified. The asymmetric velocity distribution in the columns is smoothed by the buoyancy acceleration at the boundaries. In order to compensate the rarefied northward vorticity flux in the cyclonic columns, the northward vorticity flux must be injected through the boundaries. Thus a net northward vorticity flux is generated as a result of the nonlinear coupling of the convection columns.

The results obtained in this study indicate that the convection motion in a rapidly rotating spherical shell generates a differential rotation where an equatorial acceleration takes place by the selective growth of the cyclonic convection columns.

Acknowledgements

The authors are grateful to Professor K. Nishikawa for his encouragement through out

this work. The authors are also grateful to Professor R. Horiuchi and Dr. K. Kusano for valuable discussions. This research is supported by a Grant-in-Aid from the Ministry of Education, Science and Culture in Japan.

Appendix: Numerical Techniques

There are two numerical difficulties in solving finite difference equations in the spherical coordinate system. One is the formal singularity of the equation on the poles ($\theta = 0, \pi$) and the other is the restriction of the time step which is caused by the closeness of the longitudinal grid points near the poles.

We adopt a simple way to avoid the pole singularity. Since there is no reason that the grid point must be just on the poles, we design the latitudinal (θ) grid spacing in such a way that the poles are located half way between the nearest grids, namely, the grid nearest to the north pole is $\theta = \Delta\theta/2$ and that to the south pole is $\theta = \pi - \Delta\theta/2$, where $\Delta\theta$ is the grid spacing in the direction of θ.

In order to overcome the requirement of small time step near the poles, we put a low-pass filter near the poles [12, 28]. In the spherical coordinate system, the longitudinal grid spacing $r\sin\theta\Delta\varphi$ varies drastically from the equatorial plane to the poles. The fineness of the grid spacing near the poles has an important drawback in securing the numerical accuracy, because the nonuniformity of grid spacing causes the mismatching of the phase information of the waves. In order to avoid this drawback, we adopt a remedy to filter out the redundant modes which have the shorter wavelengths than $r\Delta\varphi$. In the actual calculation, we use the Fast Fourier Transformation (FFT) at every time step to get the longitudinal mode structure at each latitude near the poles and discard the modes whose mode numbers are larger than a critical mode number. Then we make the inverse Fourier transformation to return the real space structure. The critical mode number varies with latitude. At the grid point nearest to the north pole ($\theta_1 = \Delta\theta/2$) the critical mode number is 4. Thus, all waves whose mode numbers are larger than 4 are filtered out at θ_1. (Note that, mathematically, all scalar variables must have only the zero mode number just at the pole ($\theta = 0$) and all vector variables must have the mode number 1 only.) The critical mode numbers at $\theta_2 = 3\Delta\theta/2$, $\theta_3 = 5\Delta\theta/2$, $\theta_4 = 7\Delta\theta/2$, $\theta_5 = 9\Delta\theta/2$, $\theta_6 = 11\Delta\theta/2$ and $\theta_7 = 13\Delta\theta/2$ are 13, 22, 30, 39, 47 and 56, respectively. θ_7 is about 25° in this simulation. The procedure is also applied to the southern hemisphere. For the region where $25° < \theta < (180° - 25°)$, this filtering procedure is not performed.

References

[1] F. H. Busse. *J. Fluid Mech.*, **44**, 441, 1970.

[2] F. H. Busse. *Astrophys. J.*, **159**, 629, 1970.

[3] F. H. Busse. *Astron. & Astrophys.*, **28**, 27, 1973.

[4] F. H. Busse and C. R. Carrigan. *J. Fluid Mech.*, **62**, 579, 1974.

[5] F. H. Busse and C. R. Carrigan. *Science*, **191**, 81, 1976.

[6] F. H. Busse and P. G. Cuong. *Geophys. Astrophys. Fluid Dyn.*, **8**, 17, 1977.

[7] C. R. Carrigan and F. H. Busse. *J. Fluid Mech.*, **126**, 287, 1983.

[8] J. A. Chamberlain and C. R. Carrigan. *Geophys. Astrophys. Fluid Dyn.*, **35**, 303, 1986.

[9] G. A. Glatzmaier J. E. Hart and J. Toomre. *J. Fluid Mech.*, **173**, 519, 1986.

[10] S. Cordero and F. H. Busse. *Geophys. Res. Lett.*, **19**, 733, 1992.

[11] P. A. Gilman. *J. Atmosph. Science*, **32**, 1331, 1975.

[12] P. A. Gilman. *Geophys. Astrophys. Fluid Dyn.*, **8**, 93, 1977.

[13] P. A. Gilman. *Geophys. Astrophys. Fluid Dyn.*, **11**, 157, 1978.

[14] P. A. Gilman. *Geophys. Astrophys. Fluid Dyn.*, **11**, 181, 1978.

[15] P. A. Gilman and J. Miller. *Astrophys. J. Suppl.*, **61**, 585, 1986.

[16] K. Zhang and F. H. Busse. *Geophys. Astrophys. Fluid Dyn.*, **39**, 119, 1987.

[17] K. Zhang. *Geophys. Res. Lett.*, **18**, 685, 1991.

[18] K. Zhang. *J. Fluid Mech.*, **236**, 535, 1992.

[19] P. A. Gilman and G. A. Glatzmaier. *Astrophys. J. Suppl.*, **45**, 335, 1981.

[20] E. A. Spiegel. *Astrophys. J.*, **141**, 1068, 1964.

[21] R. Horiuchi and T. Sato. *Phys. Fluid*, **B1**, 581, 1989.

[22] K. Watanabe and T. Sato. *J. Geophys. Res.*, **95**, 1990.

[23] A. S. Monin. *Theoretical geophysical fluid dynamics.* Kluwer Academic Publishers, 1988.

[24] P. A. Gilman. *Astrophys. J. Suppl.*, **53**, 243, 1983.

[25] F. H. Busse and A. C. Or. *Geophys. Astrophys. Fluid Dyn.*, **21**, 59, 1986.

[26] S. Chandrasekhar. *Hydrodynamic and Hydromagnetic Stability.* Dover, 1968.

[27] F. H. Busse and L. L. Hood. *Geophys. Astrophys. Fluid Dyn.*, **21**, 59, 1982.

[28] M. J. P. Cullen. *J. Comp. Phys.*, **50**, 1, 1983.

Figure Captions

Fig. 1: Geometry of the convection vessel (left panel) and the spherical coordinate system r (radius), θ (colatitude) and φ (longitude).

Fig. 2: Contour lines of the radial component of the velocity at the middle of the spherical shell ($r = 0.75$) for the case of $\Omega = 0$ (upper panel) and $\Omega = 0.4$ (lower panel). The solid line denotes the rising fluid and the dashed line denotes the sinking fluid.

Fig. 3: Time development of the total energy (solid thick line), the differential rotation kinetic energy (thin line) and the helicity (dashed line) for the case of $\Omega = 0.4$. The left side scale is for the energy and the right side scale is for the helicity.

Fig. 4: Contour lines of the temperature (upper left panel), density (upper right), latitudinal component of the vorticity (lower left) and the pressure perturbation (lower right panel) in the equatorial plane. The solid contour denotes the positive value and the dashed contour denotes the negative value. The spherical shell rotates in the counterclockwise direction in this figure.

Fig. 5: Time development of the convection pattern in the middle of the spherical shell ($r = 0.75$).

Fig. 6: Power spectra of the longitudinal mode of the radial component velocity v_r at the equator at 30,000 time steps (upper panel) and 300,000 time steps (lower panel).

Fig. 7: Time development of the longitudinal modes of the radial component velocity v_r at the equator.

Fig. 8: Time development of the convection columns. The black (white) regions correspond to the regions where the fluid rises (sinks) at the middle of the shell in the equatorial plane ($r = 0.75$).

Fig. 9: Flow distributions of the horizontal component (upper panel) and the radial component (lower panel) of the velocity on a spherical surface near the outer boundary ($r = 0.9$) at 300,000 time steps. The solid line denotes the rising part of the fluid and the dashed line denotes the sinking part.

Fig. 10: Flow distributions of the velocity vectors in the equatorial plane ($\theta = 90°$) and in the plane ($\theta = 70°$) at 300,000 time steps. The contour line on the right shows

the latitudinal component of the velocity v_θ where the solid line denotes the positive v_θ (southward) and the dashed line denotes the negative v_θ (northward). The spherical shell rotates counterclockwise.

Fig. 11: Three-dimensional display of a flow line viewed from $\theta = 0°$ (upper left), $\theta = 30°$ (upper right), $\theta = 60°$ (lower left) and $\theta = 90°$ (lower right). The color plot in the equatorial plane indicates the intensity of the latitudinal vorticity ω_θ. The red expresses the positive and the blue the negative. The brown sphere denotes the inner boundary.

Fig. 12: Contour lines of the longitudinally averaged kinetic helicity density (left) and the differential rotation (right) in a meridional plane at $300,000$ time steps for $\Omega = 0.4$. The solid line denotes the positive value and the dashed line denotes the negative value.

Fig. 13: Differential rotation as a function of the latitude. The horizontal axis is $\overline{v}_\varphi$ and the vertical axis is the colatitude.

Fig. 14: Contour lines of the mean helicity density (left) and the differential rotation (right) in a meridional plane for $\Omega = 0.2$.

Fig. 15: Contour lines of the mean helicity density (left) and the differential rotation (right) in a meridional plane for $\Omega = 0.1$.

Fig. 16: Schematic diagram of three patterns of the convection columns in the equatorial plane.

Fig. 17: Contour lines of the mean vorticity in a meridional plane at $300,000$ time steps for $\Omega = 0.4$.

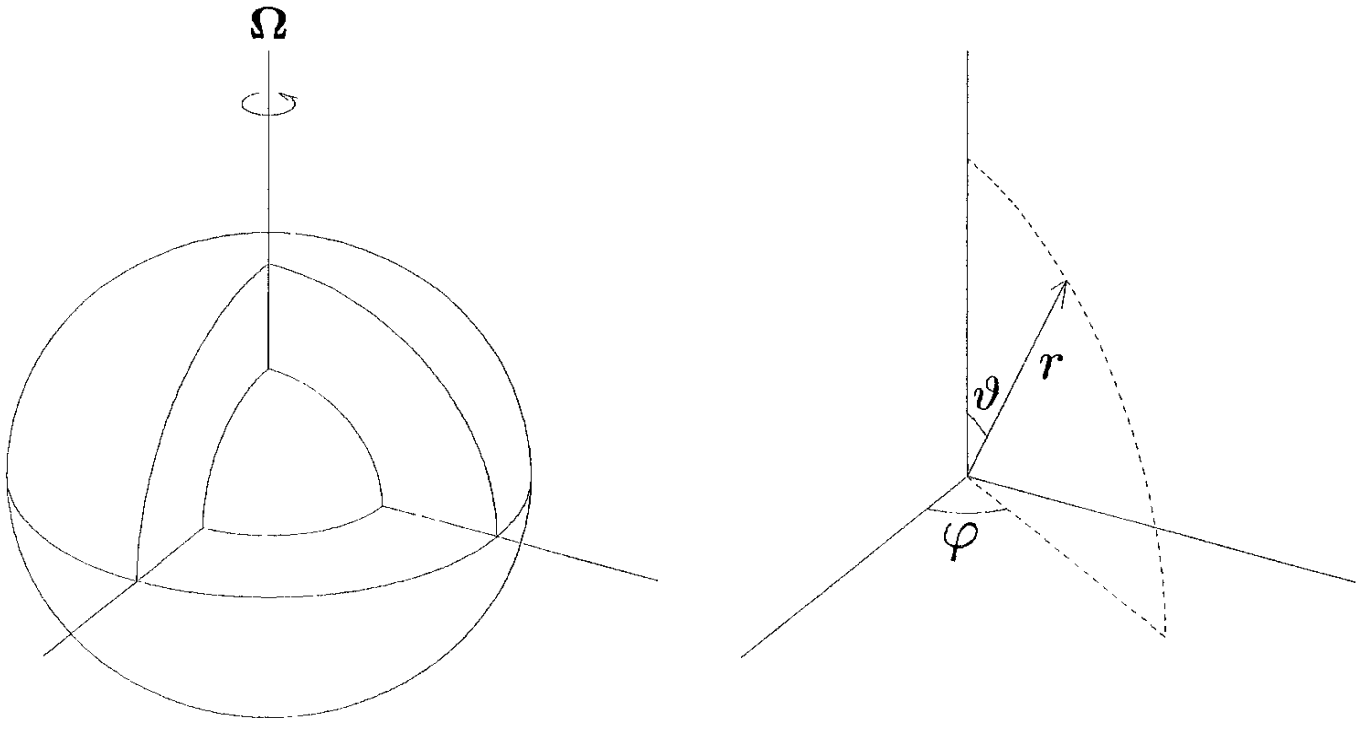

Fig. 1

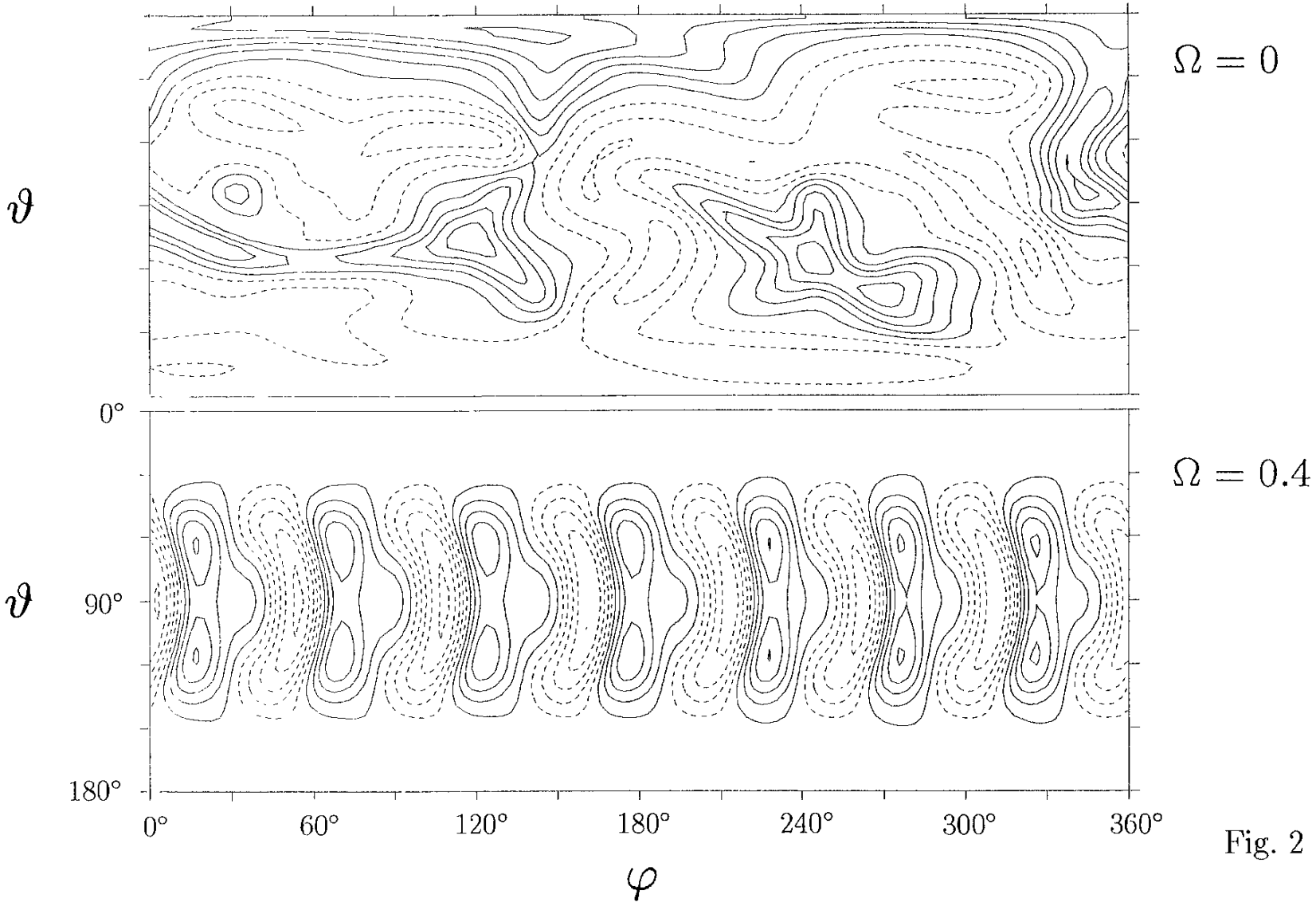
Radial Velocity at $r = 0.75$
$\Omega = 0$
$\Omega = 0.4$
ϑ
ϑ
0°
90°
180°
0°
60°
120°
180°
240°
300°
360°
φ

Fig. 2

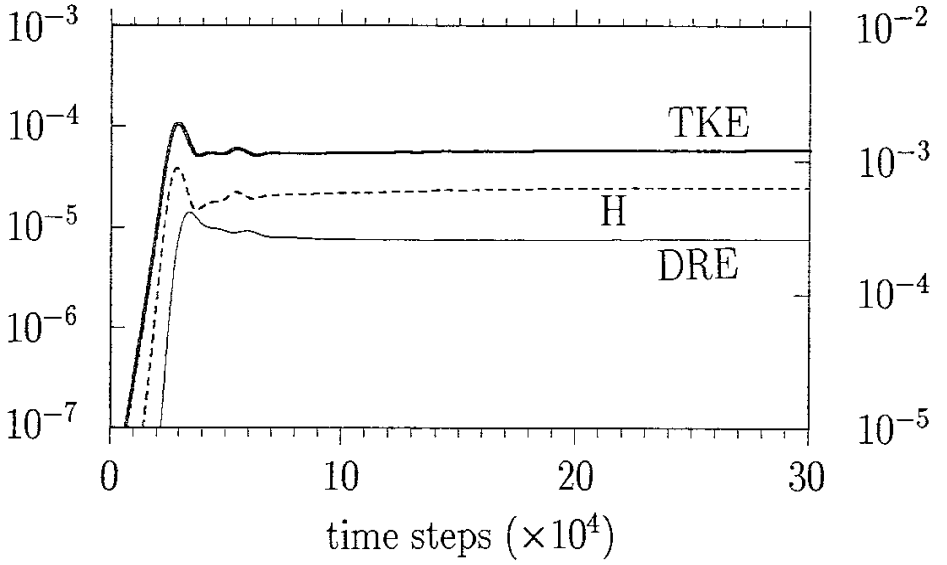
10^{-3}
10^{-4}
10^{-5}
10^{-6}
10^{-7}
10^{-2}
10^{-3}
10^{-4}
10^{-5}
TKE
H
DRE
0
10
20
30
time steps ($\times 10^4$)

Fig. 3

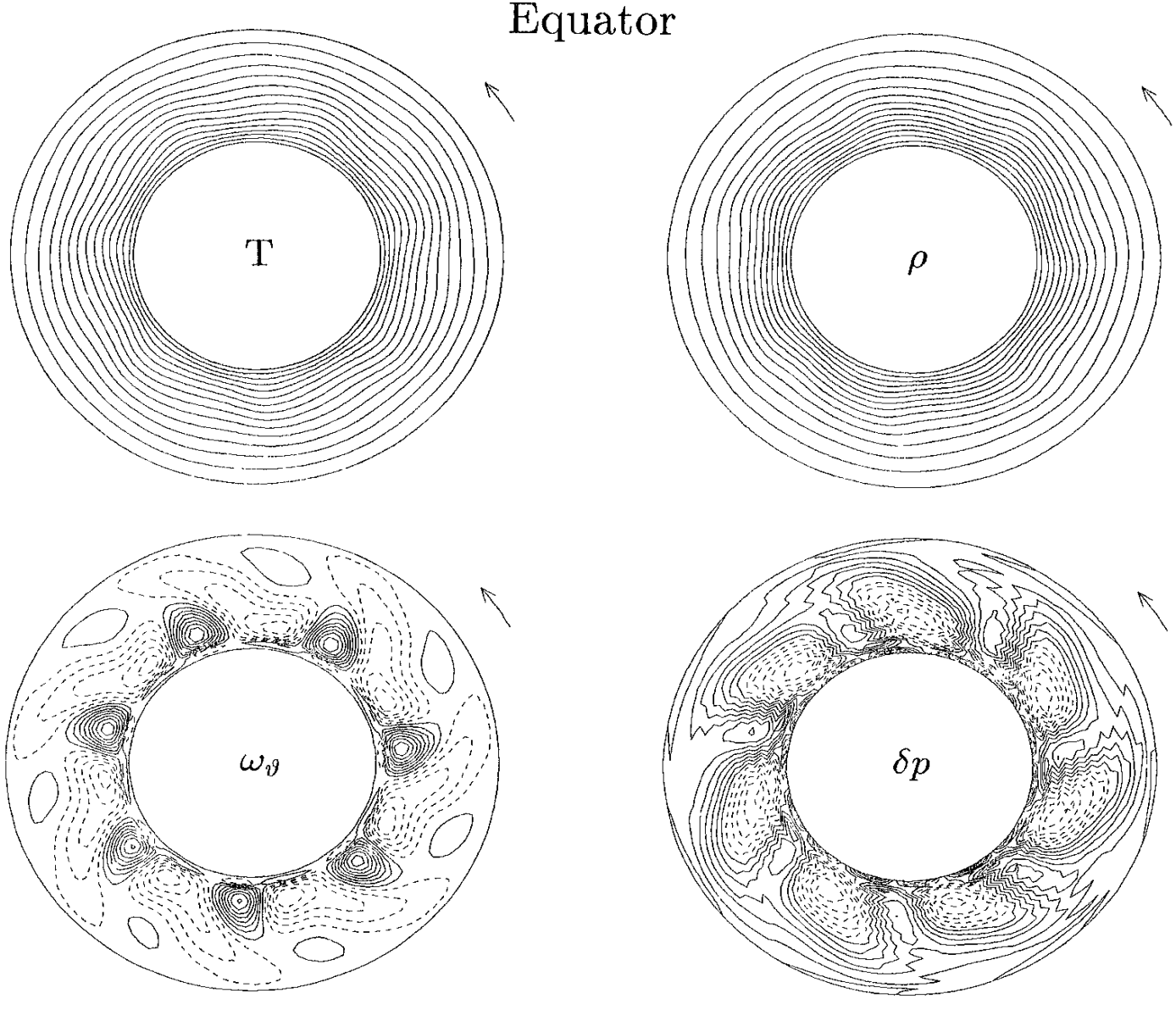

Fig. 4

Radial Velocty at $r = 0.75$

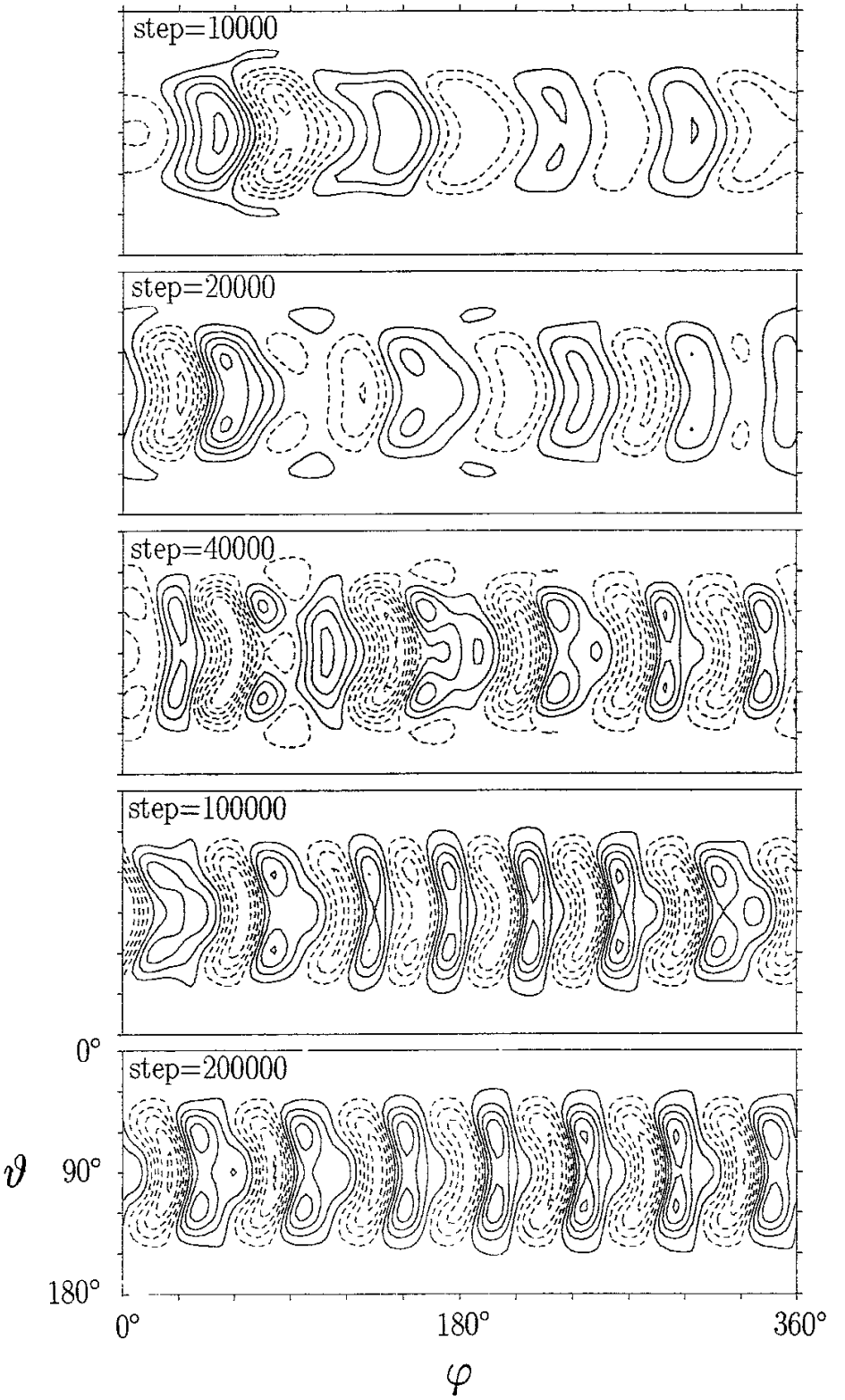

Fig. 5

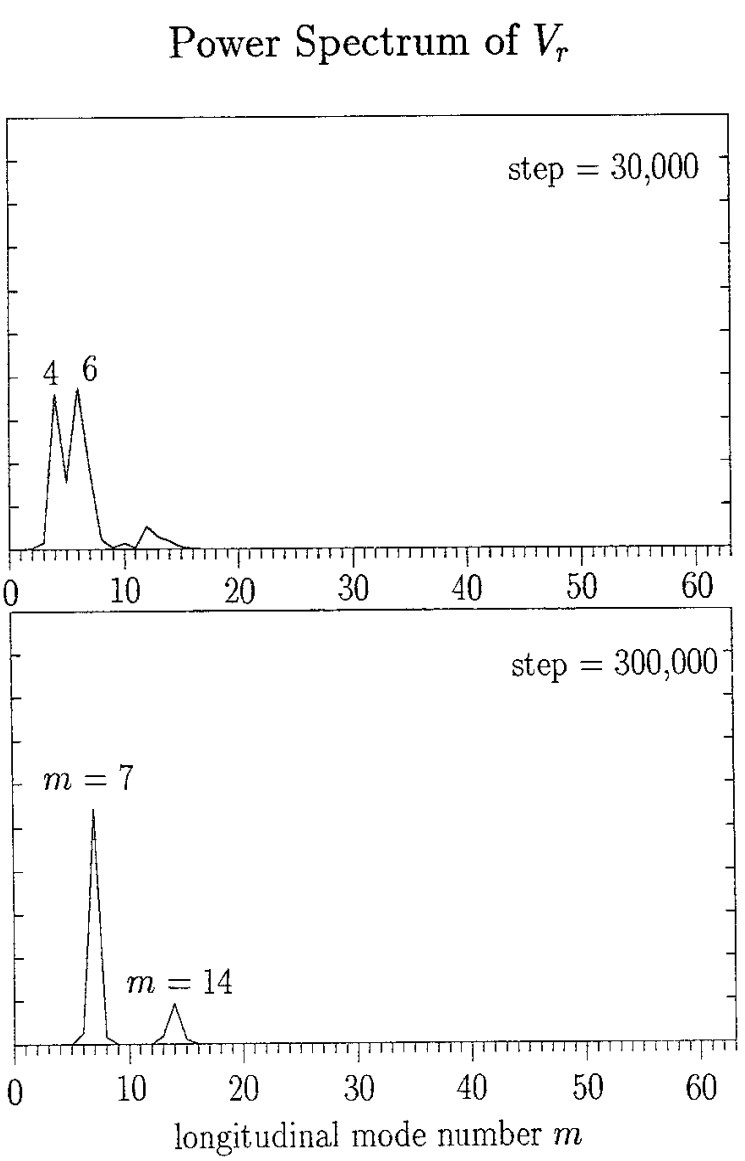
Power Spectrum of V_r
step = 30,000
4
6
0
10
20
30
40
50
60
step = 300,000
$m = 7$
$m = 14$
0
10
20
30
40
50
60
longitudinal mode number m

Fig. 6

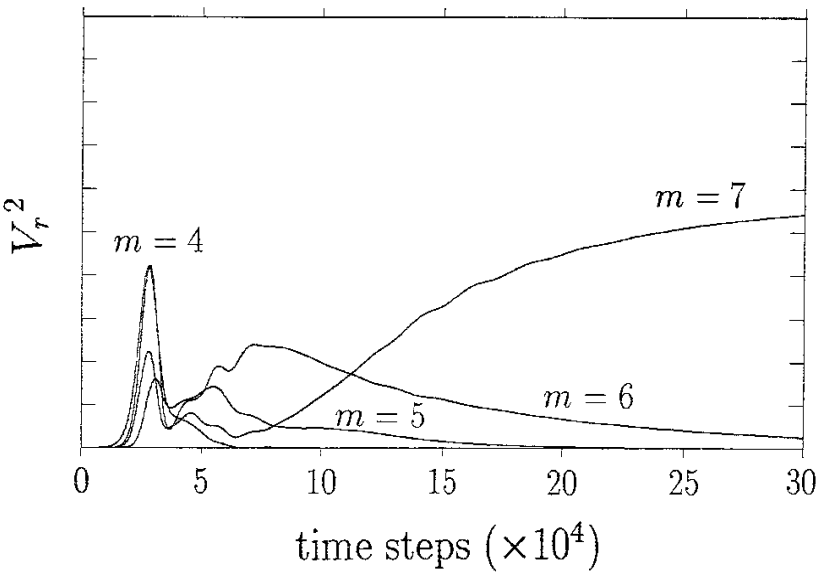

Fig. 7

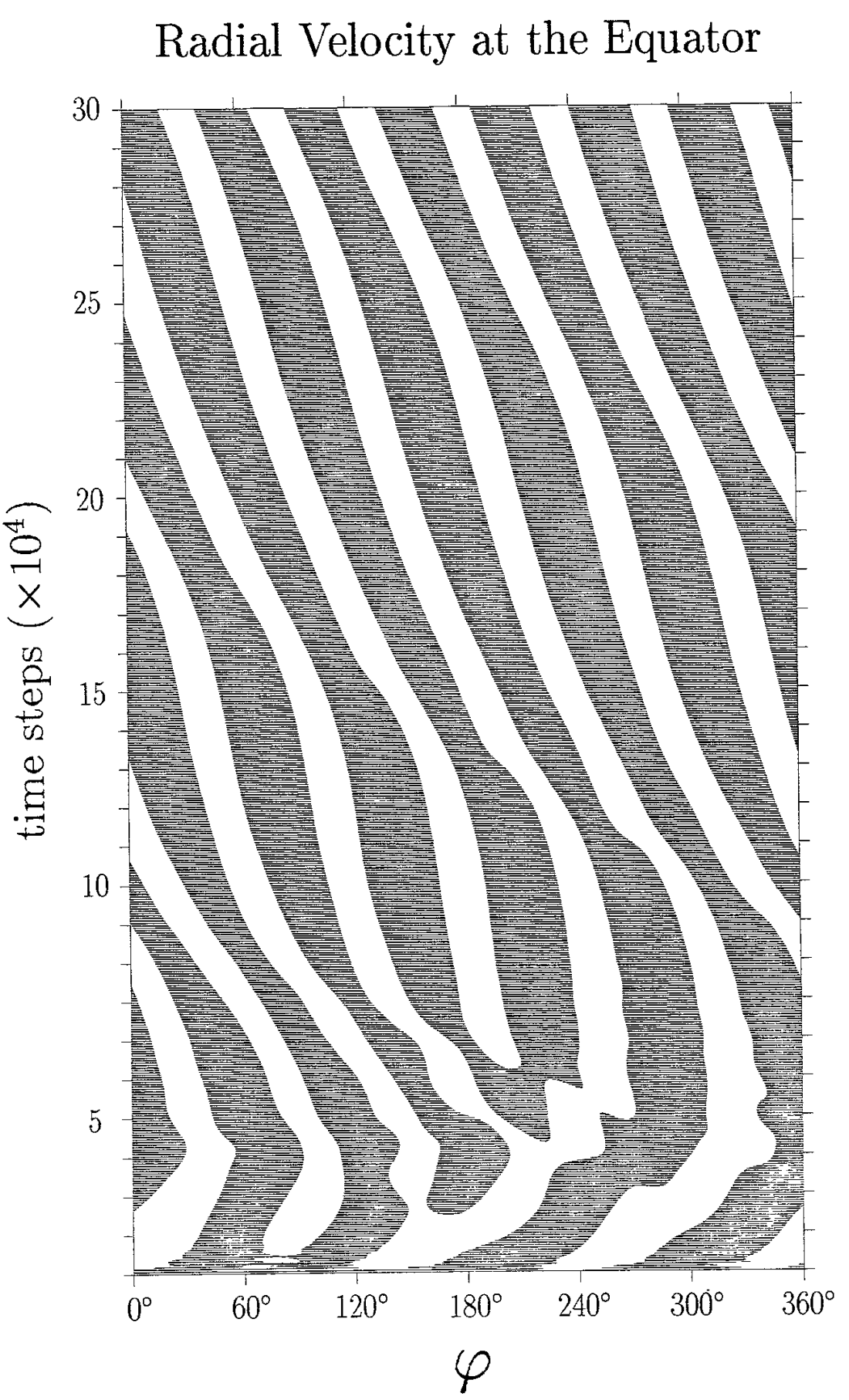
Radial Velocity at the Equator
30
25
20
15
10
5
time steps ($\times 10^4$)
0°
60°
120°
180°
240°
300°
360°
φ

Fig. 8

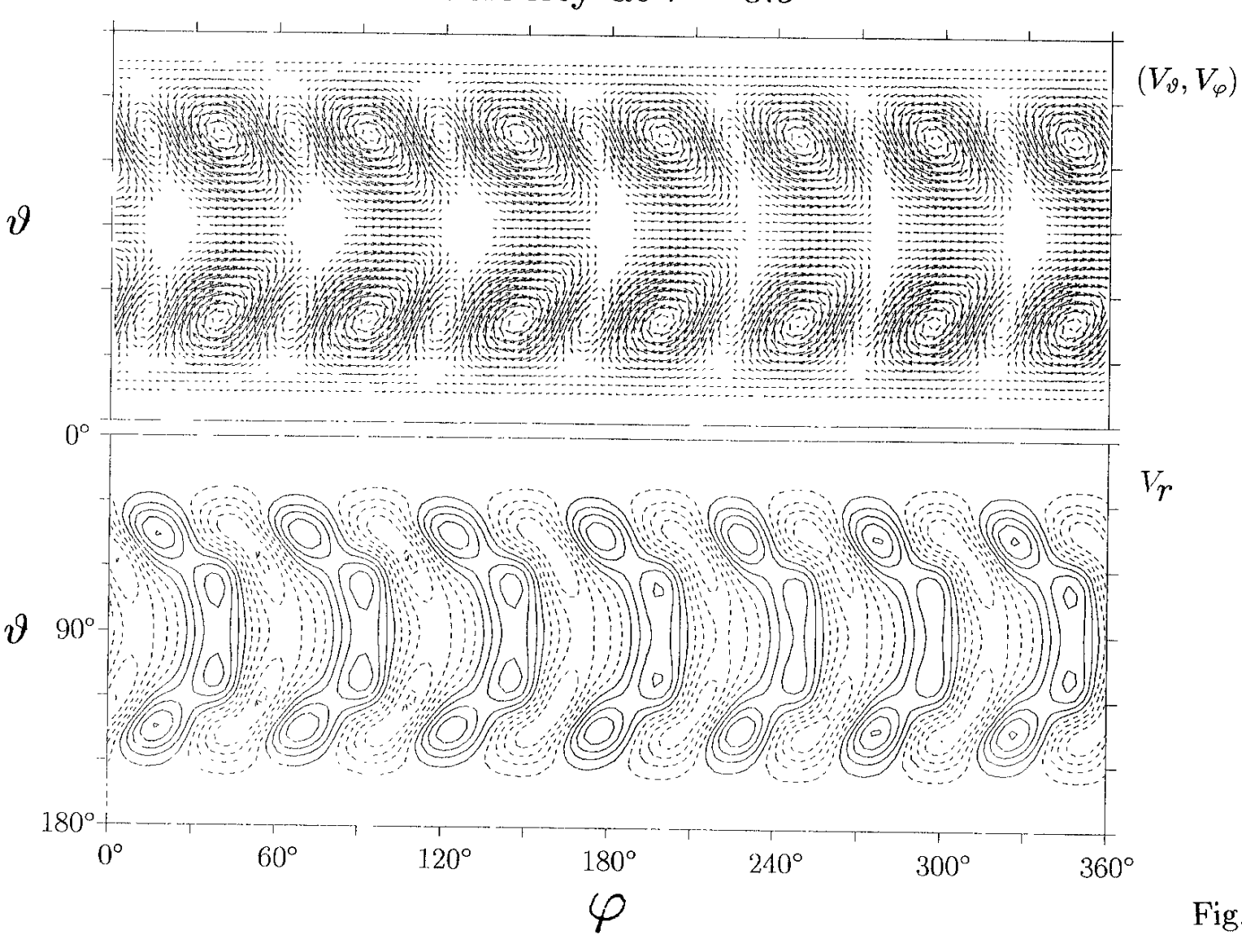
Velocity at $r = 0.9$
(V_ϑ, V_φ)
ϑ
0°
V_r
ϑ
90°
180°
0°
60°
120°
180°
240°
300°
360°
φ

Fig. 9

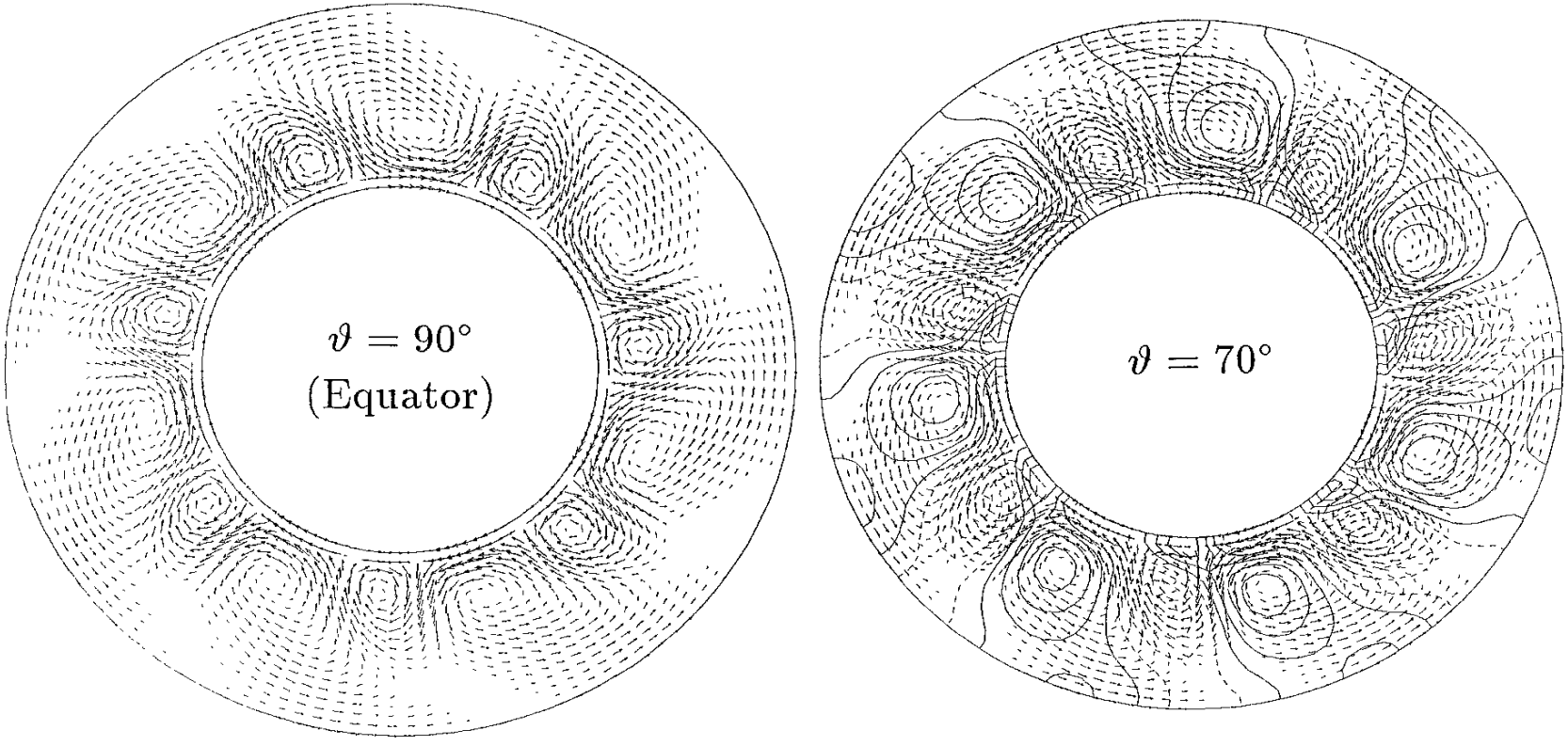

Fig. 10

Vorticity in the Equatorial Plane and Flow line

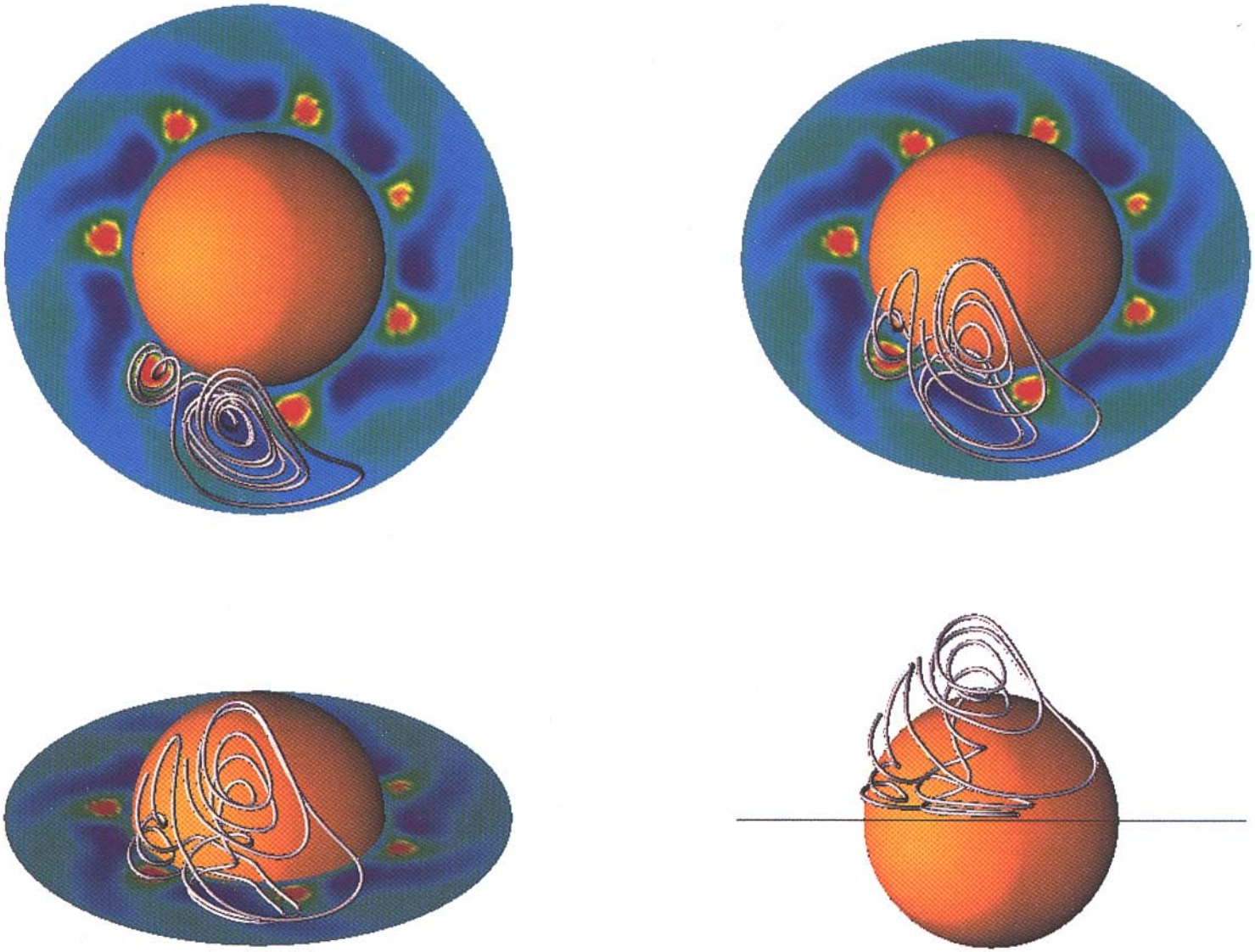

Fig. 11

Helicity

Differential Rotation

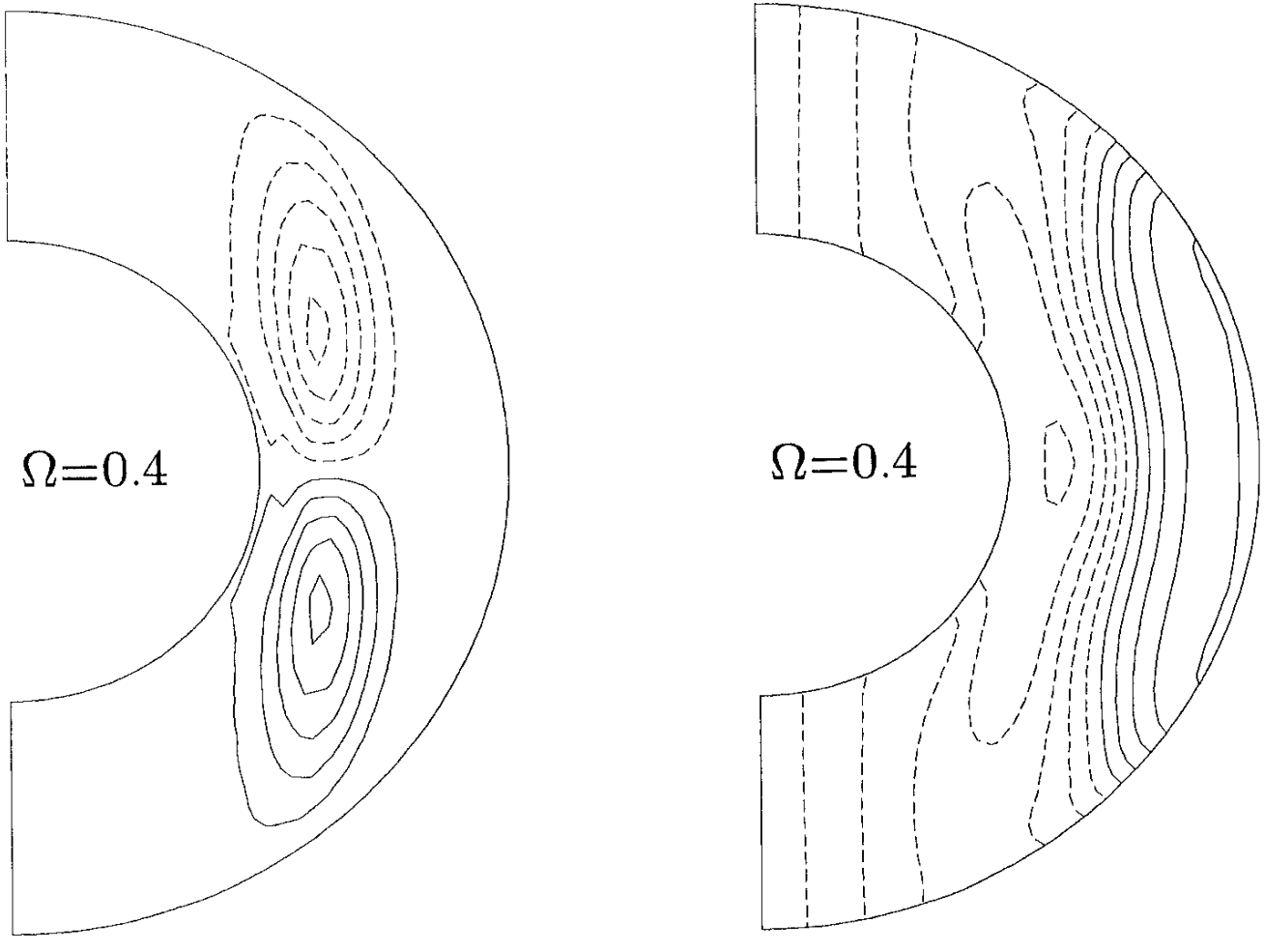

Fig. 12

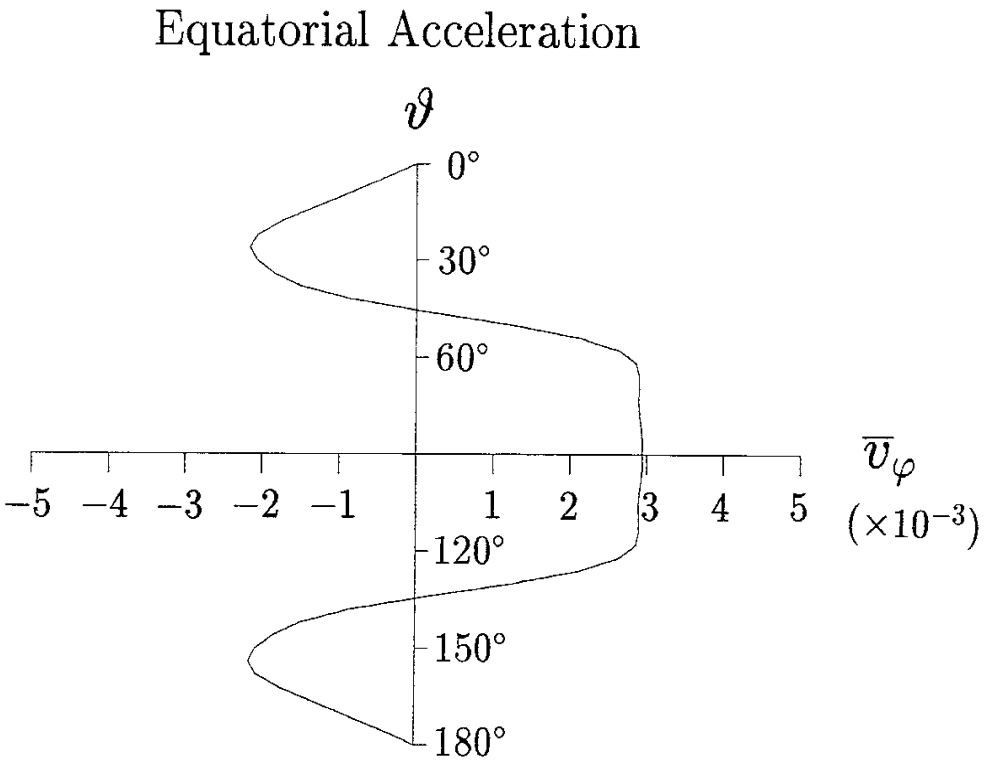
Equatorial Acceleration
ϑ
0°
30°
60°
120°
150°
180°
−5 −4 −3 −2 −1 1 2 3 4 5
$\overline{v}_\varphi$
$(\times 10^{-3})$

Fig. 13

Helicity

Differential Rotation

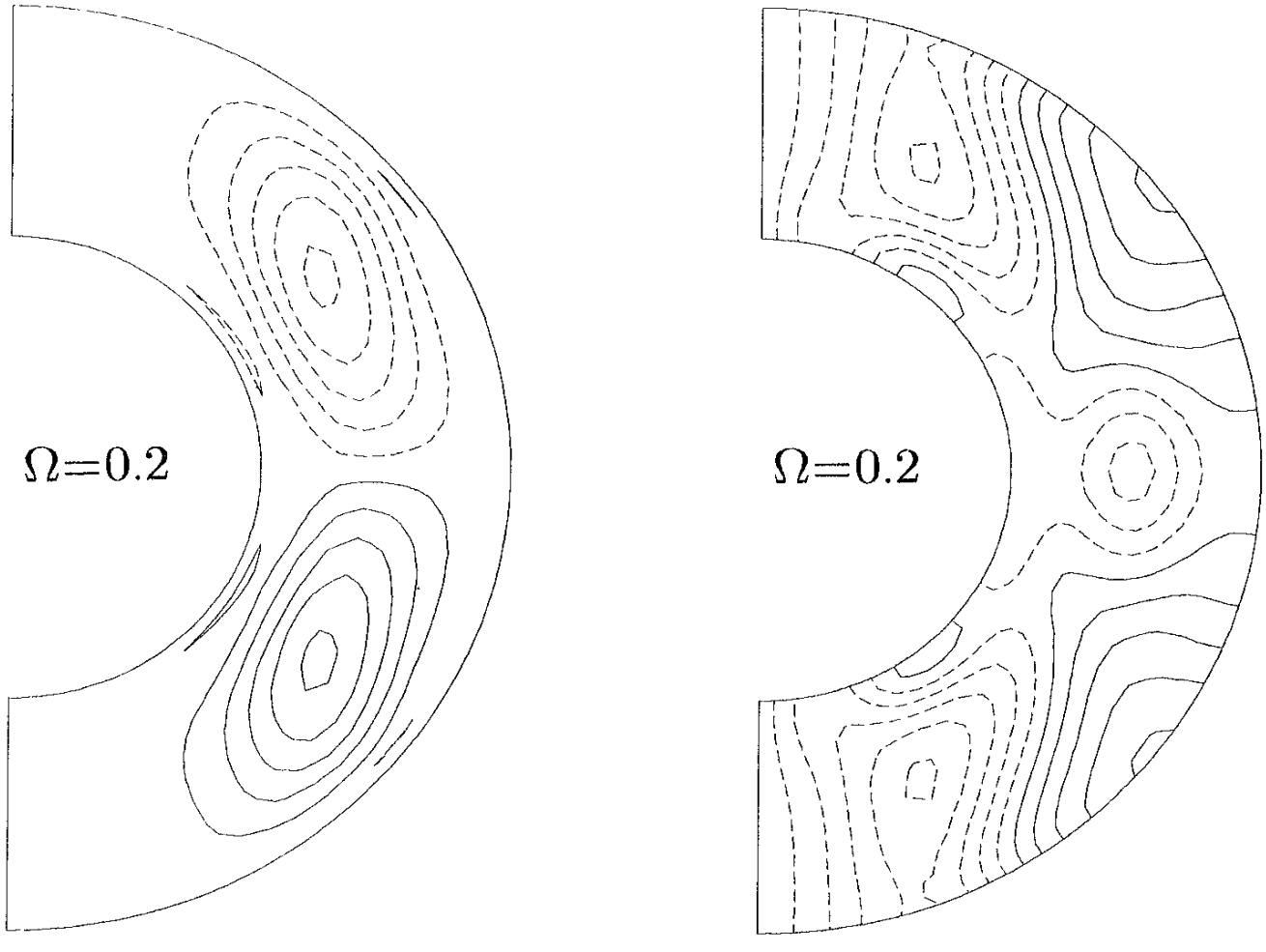

Fig. 14

Helicity

Differential Rotation

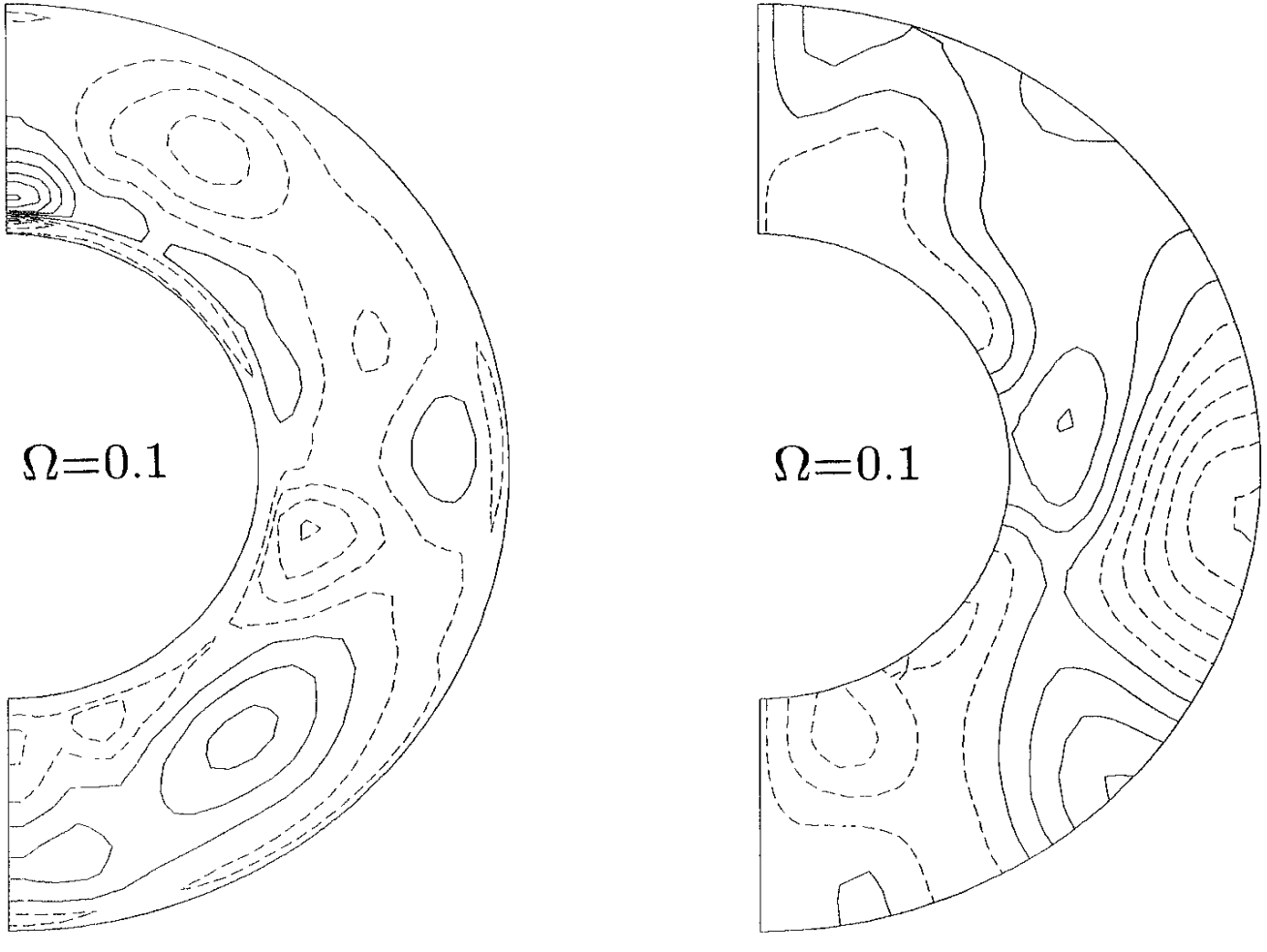

Fig. 15

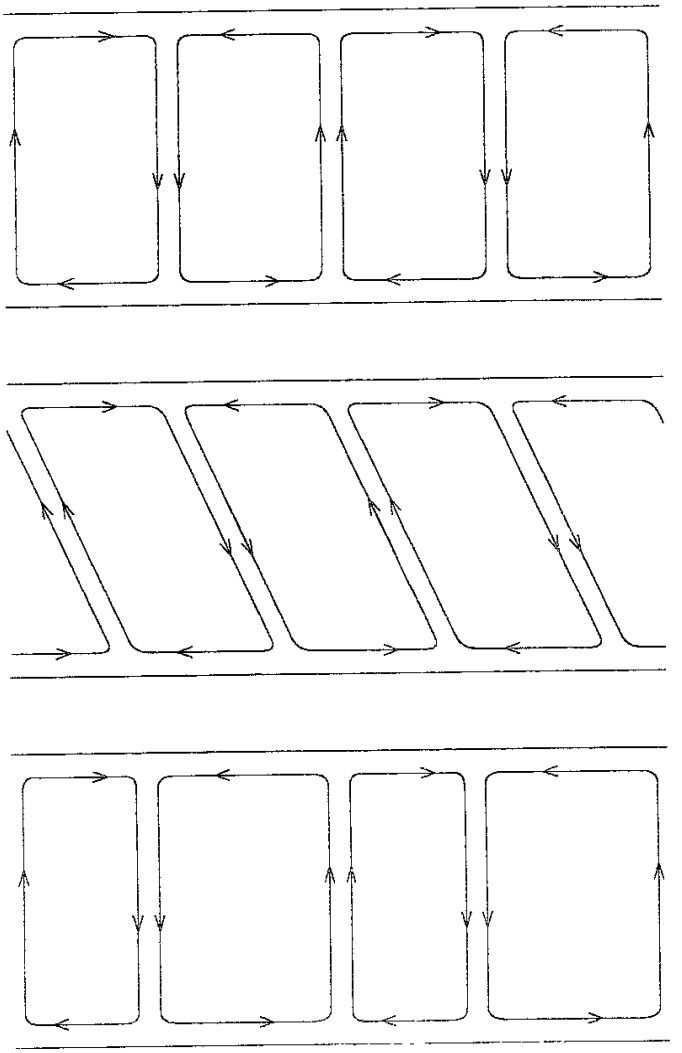

Fig. 16

Averaged Vorticity

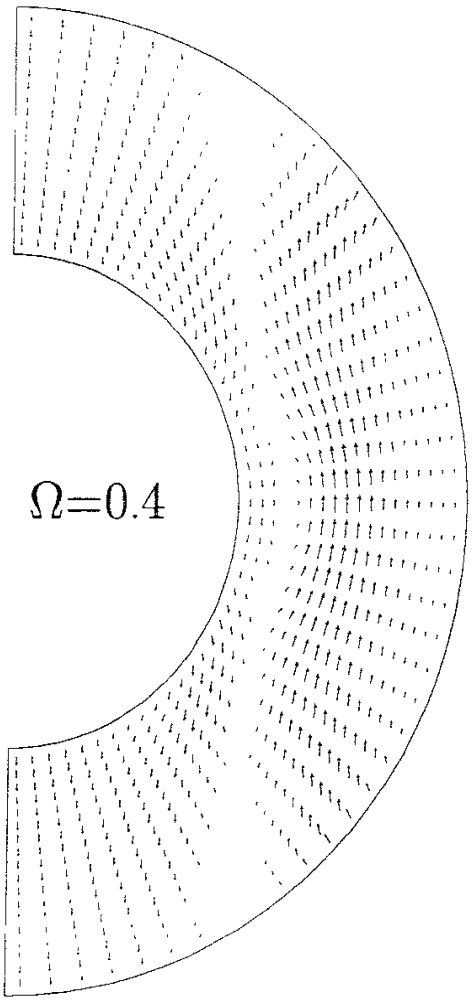

Fig. 17

Recent Issues of NIFS Series

NIFS-165 T. Seki, R. Kumazawa, T. Watari, M. Ono, Y. Yasaka, F. Shimpo, A. Ando, O. Kaneko, Y. Oka, K. Adati, R. Akiyama, Y. Hamada, S. Hidekuma, S. Hirokura, K. Ida, A. Karita, K. Kawahata, Y. Kawasumi, Y. Kitoh, T. Kohmoto, M. Kojima, K. Masai, S. Morita, K. Narihara, Y. Ogawa, K. Ohkubo, S. Okajima, T. Ozaki, M. Sakamoto, M. Sasao, K. Sato, K. N. Sato, H. Takahashi, Y. Taniguchi, K. Toi and T. Tsuzuki, *High Frequency Ion Bernstein Wave Heating Experiment on JIPP T-IIU Tokamak*; Aug. 1992

NIFS-166 Vo Hong Anh and Nguyen Tien Dung, *A Synergetic Treatment of the Vortices Behaviour of a Plasma with Viscosity*; Sep. 1992

NIFS-167 K. Watanabe and T. Sato, *A Triggering Mechanism of Fast Crash in Sawtooth Oscillation*; Sep. 1992

NIFS-168 T. Hayashi, T. Sato, W. Lotz, P. Merkel, J. Nührenberg, U. Schwenn and E. Strumberger, *3D MHD Study of Helias and Heliotron;* Sep. 1992

NIFS-169 N. Nakajima, K. Ichiguchi, K. Watanabe, H. Sugama, M. Okamoto, M. Wakatani, Y. Nakamura and C. Z. Cheng, *Neoclassical Current and Related MHD Stability, Gap Modes, and Radial Electric Field Effects in Heliotron and Torsatron Plasmas;* Sep. 1992

NIFS-170 H. Sugama, M. Okamoto and M. Wakatani, *K- ε Model of Anomalous Transport in Resistive Interchange Turbulence* ; Sep, 1992

NIFS-171 H. Sugama, M. Okamoto and M. Wakatani, *Vlasov Equation in the Stochastic Magnetic Field* ; Sep. 1992

NIFS-172 N. Nakajima, M. Okamoto and M. Fujiwara, *Physical Mechanism of E_ϕ-Driven Current in Asymmetric Toroidal Systems* ; Sep.1992

NIFS-173 N. Nakajima, J. Todoroki and M. Okamoto, *On Relation between Hamada and Boozer Magnetic Coordinate System* ; Sep. 1992

NIFS-174 K. Ichiguchi, N. Nakajima, M. Okamoto, Y. Nakamura and M. Wakatani, *Effects of Net Toroidal Current on Mercier Criterion in the Large Helical Device* ; Sep. 1992

NIFS-175 S. -I. Itoh, K. Itoh and A. Fukuyama, *Modelling of ELMs and Dynamic Responses of the H-Mode* ; Sep. 1992

NIFS-176 K. Itoh, S.-I. Itoh, A. Fukuyama, H. Sanuki, K. Ichiguchi and J. Todoroki, *Improved Models of β-Limit, Anomalous Transport*

and Radial Electric Field with Loss Cone Loss in Heliotron / Torsatron ; Sep. 1992

NIFS-177 N. Ohyabu, K. Yamazaki, I. Katanuma, H. Ji, T. Watanabe, K. Watanabe, H. Akao, K. Akaishi, T. Ono, H. Kaneko, T. Kawamura, Y. Kubota, N. Noda, A. Sagara, O. Motojima, M. Fujiwara and A. Iiyoshi, *Design Study of LHD Helical Divertor and High Temperature Divertor Plasma Operation* ; Sep. 1992

NIFS-178 H. Sanuki, K. Itoh and S.-I. Itoh, *Selfconsistent Analysis of Radial Electric Field and Fast Ion Losses in CHS Torsatron / Heliotron* ; Sep. 1992

NIFS-179 K. Toi, S. Morita, K. Kawahata, K. Ida, T. Watari, R. Kumazawa, A. Ando, Y. Oka, K. Ohkubo, Y. Hamada, K. Adati, R. Akiyama, S. Hidekuma, S. Hirokura, O. Kaneko, T. Kawamoto, Y. Kawasumi, M. Kojima, T. Kuroda, K. Masai, K. Narihara, Y. Ogawa, S. Okajima, M. Sakamoto, M. Sasao, K. Sato, K. N. Sato, T. Seki, F. Shimpo, S. Tanahashi, Y. Taniguchi, T. Tsuzuki, *New Features of L-H Transition in Limiter H-Modes of JIPP T-IIU* ; Sep. 1992

NIFS-180 H. Momota, Y. Tomita, A. Ishida, Y. Kohzaki, M. Ohnishi, S. Ohi, Y. Nakao and M. Nishikawa, *D-^{3}He Fueled FRC Reactor "Artemis-L"* ; Sep. 1992

NIFS-181 T. Watari, R. Kumazawa, T. Seki, Y. Yasaka, A. Ando, Y. Oka,O. Kaneko, K. Adati, R. Akiyama, Y. Hamada, S. Hidekuma, S. Hirokura, K. Ida, K. Kawahata, T. Kawamoto, Y. Kawasumi, S. Kitagawa, M. Kojima, T. Kuroda, K. Masai, S. Morita, K. Narihara, Y. Ogawa, K. Ohkubo, S. Okajima, T. Ozaki, M. Sakamoto, M. Sasao, K. Sato, K. N. Sato, F.Shimpo, H. Takahashi, S. Tanahasi, Y. Taniguchi, K. Toi, T. Tsuzuki and M. Ono, *The New Features of Ion Bernstein Wave Heating in JIPP T-IIU Tokamak* ;Sep, 1992

NIFS-182 K. Itoh, H. Sanuki and S.-I. Itoh, *Effect of Alpha Particles on Radial Electric Field Structure in Torsatron / Heliotron Reactor*; Sep. 1992

NIFS-183 S. Morimoto, M. Sato, H. Yamada, H. Ji, S. Okamura, S. Kubo, O. Motojima, M. Murakami, T. C. Jernigan, T. S. Bigelow, A. C. England, R. S. Isler, J. F. Lyon, C. H. Ma, D. A. Rasmussen, C. R. Schaich, J. B. Wilgen and J. L. Yarber, *Long Pulse Discharges Sustained by Second Harmonic Electron Cyclotron Heating Using a 35GH$_Z$ Gyrotron in the Advanced Toroidal Facility*; Sep. 1992

NIFS-184 S. Okamura, K. Hanatani, K. Nishimura, R. Akiyama, T. Amano, H. Arimoto, M. Fujiwara, M. Hosokawa, K. Ida, H. Idei, H. Iguchi, O. Kaneko, T. Kawamoto, S. Kubo, R. Kumazawa, K. Matsuoka, S. Morita, O. Motojima, T. Mutoh, N. Nakajima, N. Noda, M. Okamoto, T. Ozaki, A. Sagara, S. Sakakibara, H. Sanuki, T. Seki, T. Shoji,

F. Shimbo, C. Takahashi, Y. Takeiri, Y. Takita, K. Toi, K. Tsumori, M. Ueda, T. Watari, H. Yamada and I. Yamada, *Heating Experiments Using Neutral Beams with Variable Injection Angle and ICRF Waves in CHS* ; Sep. 1992

NIFS-185 H. Yamada, S. Morita, K. Ida, S. Okamura, H. Iguchi, S. Sakakibara, K. Nishimura, R. Akiyama, H. Arimoto, M. Fujiwara, K. Hanatani, S. P. Hirshman, K. Ichiguchi, H. Idei, O. Kaneko, T. Kawamoto, S. Kubo, D. K. Lee, K. Matsuoka, O, Motojima, T. Ozaki, V. D. Pustovitov, A. Sagara, H. Sanuki, T. Shoji, C. Takahashi, Y. Takeiri, Y. Takita, S. Tanahashi, J. Todoroki, K. Toi, K. Tsumori, M. Ueda and I. Yamada, *MHD and Confinement Characteristics in the High-β Regime on the CHS Low-Aspect-Ratio Heliotron / Torsatron* ; Sep. 1992

NIFS-186 S. Morita, H. Yamada, H. Iguchi, K. Adati, R. Akiyama, H. Arimoto, M. Fujiwara, Y. Hamada, K. Ida, H. Idei, O. Kaneko, K. Kawahata, T. Kawamoto, S. Kubo, R. Kumazawa, K. Matsuoka, T. Morisaki, K. Nishimura, S. Okamura, T. Ozaki, T. Seki, M. Sakurai, S, Sakakibara, A. Sagara, C. Takahashi, Y. Takeiri, H. Takenaga, Y. Takita, K. Toi, K. Tsumori, K. Uchino, M. Ueda, T. Watari, I. Yamada, *A Role of Neutral Hydrogen in CHS Plasmas with Reheat and Collapse and Comparison with JIPP T-IIU Tokamak Plasmas* ; Sep. 1992

NIFS-187 K. Ioth, S.-I. Itoh, A. Fukuyama, M. Yagi and M. Azumi, *Model of the L-Mode Confinement in Tokamaks* ; Sep. 1992

NIFS-188 K. Itoh, A. Fukuyama and S.-I. Itoh, *Beta-Limiting Phenomena in High-Aspect-Ratio Toroidal Helical Plasmas*; Oct. 1992

NIFS-189 K. Itoh, S. -I. Itoh and A. Fukuyama, *Cross Field Ion Motion at Sawtooth Crash* ; Oct. 1992

NIFS-190 N. Noda, Y. Kubota, A. Sagara, N. Ohyabu, K. Akaishi, H. Ji, O. Motojima, M. Hashiba, I. Fujita, T. Hino, T. Yamashina, T. Matsuda, T. Sogabe, T. Matsumoto, K. Kuroda, S. Yamazaki, H. Ise, J. Adachi and T. Suzuki, *Design Study on Divertor Plates of Large Helical Device (LHD)* ; Oct. 1992

NIFS-191 Y. Kondoh, Y. Hosaka and K. Ishii, *Kernel Optimum Nearly-Analytical Discretization (KOND) Algorithm Applied to Parabolic and Hyperbolic Equations* : Oct. 1992

NIFS-192 K. Itoh, M. Yagi, S.-I. Itoh, A. Fukuyama and M. Azumi, *L-Mode Confinement Model Based on Transport-MHD Theory in Tokamaks* ; Oct. 1992

NIFS-193 T. Watari, *Review of Japanese Results on Heating and Current*

Drive ; Oct. 1992

NIFS-194 Y. Kondoh, *Eigenfunction for Dissipative Dynamics Operator and Attractor of Dissipative Structure* ; Oct. 1992

NIFS-195 T. Watanabe, H. Oya, K. Watanabe and T. Sato, *Comprehensive Simulation Study on Local and Global Development of Auroral Arcs and Field-Aligned Potentials* ; Oct. 1992

NIFS-196 T. Mori, K. Akaishi, Y. Kubota, O. Motojima, M. Mushiaki, Y. Funato and Y. Hanaoka, *Pumping Experiment of Water on B and LaB_6 Films with Electron Beam Evaporator* ; Oct., 1992

NIFS-197 T. Kato and K. Masai, *X-ray Spectra from Hinotori Satellite and Suprathermal Electrons* ; Oct. 1992

NIFS-198 K. Toi, S. Okamura, H. Iguchi, H. Yamada, S. Morita, S. Sakakibara, K. Ida, K. Nishimura, K. Matsuoka, R. Akiyama, H. Arimoto, M. Fujiwara, M. Hosokawa, H. Idei, O. Kaneko, S. Kubo, A. Sagara, C. Takahashi, Y. Takeiri, Y. Takita, K. Tsumori, I. Yamada and H. Zushi, *Formation of H-mode Like Transport Barrier in the CHS Heliotron / Torsatron* ; Oct. 1992

NIFS-199 M. Tanaka, *A Kinetic Simulation of Low-Frequency Electromagnetic Phenomena in Inhomogeneous Plasmas of Three-Dimensions* ; Nov. 1992

NIFS-200 K. Itoh, S.-I. Itoh, H. Sanuki and A. Fukuyama, *Roles of Electric Field on Toroidal Magnetic Confinement*, Nov. 1992

NIFS-201 G. Gnudi and T. Hatori, *Hamiltonian for the Toroidal Helical Magnetic Field Lines in the Vacuum*; Nov. 1992

NIFS-202 K. Itoh, S.-I. Itoh and A. Fukuyama, *Physics of Transport Phenomena in Magnetic Confinement Plasmas*; Dec. 1992

NIFS-203 Y. Hamada, Y. Kawasumi, H. Iguchi, A. Fujisawa, Y. Abe and M. Takahashi, *Mesh Effect in a Parallel Plate Analyzer*; Dec. 1992

NIFS-204 T. Okada and H. Tazawa, *Two-Stream Instability for a Light Ion Beam -Plasma System with External Magnetic Field;* Dec. 1992

NIFS-205 M. Osakabe, S. Itoh, Y. Gotoh, M. Sasao and J. Fujita, *A Compact Neutron Counter Telescope with Thick Radiator (Cotetra) for Fusion Experiment*; Jan. 1993

NIFS-206 T. Yabe and F. Xiao, *Tracking Sharp Interface of Two Fluids by the CIP (Cubic-Interpolated Propagation) Scheme*, Jan. 1993